CARBO-NITRIDE PRECIPITATION AND ITS EFFECTS ON MATRIX TRANSFORMATIONS IN HIGH-STRENGTH / HIGH-TOUGHNESS 300M STEEL

by

ANCA MARILENA JUBLEANU

A thesis submitted to
The University of Birmingham
for the degree of
MASTER OF RESEARCH

Department of Metallurgy and Materials
The University of Birmingham
September 2009

ACKNOWLEDGEMENTS

I am grateful to my supervisors Dr. Martin Strangwood and Dr. Claire Davis, without whom I would not have been able to complete the project.

I also felt supported by the friendship of the students in my group, particularly, Amrita.

I would like to thank the Department of Metallurgy and Materials for the sponsorship of the project and the fact that I have been able to use the facilities of the university.

ABSTRACT

The influences of different austenitisation temperatures on the matrix microstructure and mechanical properties (K_{1C} and hardness) of one cast have been investigated.

300M steel has been austenitised at 925 °C for increasing holding times from 1h to 4h and 1025 °C for 2h holding time.

Microstructures were examined by optical and scanning electron microscopy.

It has been found out that higher austenitisation temperature alter the microstructure, the fine (<600 nm) precipitate population and subsequently the fracture toughness.

The reduced volume fraction of fine particles increased the hardenability of the steel, resulting in an increased percentage of upper bainite, that led to a lower temper response compared to 925 austenitisation temperature.

The improved K_{1C} value was attributed to increased dissolution of fine particles due to higher austenitisation temperatures.

CONTENTS

CHAPTER 1

Introduction

The use of commercial ultrahigh – strength levels of medium carbon alloyed steels has increased in critical structural aircraft and aerospace applications under severely stressed situations, as a result, these steels require better ductility and toughness as well as higher strength.

The AISI 4340 steel has been developed since 1950 and has been used in commercial practice since 1955. In order to meet the severe requirements of high strength and stiffness, together with low volume and weight, ultrahigh strength 300M steel was introduced as a higher strength replacement to 4340 steel, being employed in critical components of aircraft lending gear since 1966. The mechanical properties of this steel have been modified by adding silicon and vanadium alloying elements to 4340 steel.

300M achieves high strength by a fine array of alloy carbides in a bainitic / tempered martensite matrix, Si additions favouring retained austenite over cementite resulting in high toughness. The mechanical properties (strength and toughness) are strongly dependent on both the precipitate distributions and matrix phase balance, which are interrelated and controlled through a series of thermomechanical processes.

Previous studies characterised the effects of composition (mainly Ti varaiations) and processing parameters on particle distributions. The aim of this project is to analyse the effects of heating to and cooling from different austenitisation temperatures on particle distributions and resultant microstructures then correlating them with mechanical properties (hardness and toughness).

CHAPTER 2

The Physical Metallurgy of High Strength Steel

2.1 Strengthening Mechanisms in Steel

High strength steels have generally been used in quenched and tempered conditions. The use of these steels in critical structural applications under severely stressed situations requires greater ductility and toughness as well as higher strength [Tomita, 1995]. The addition of alloying elements increases the hardenability of the steel so that less severe quenching rates can be used reducing the risk of distortion and quench cracking associated with rapid quenching.

The addition of alloying elements gives increased strengthening through: grain refinement, solid solution strengthening and precipitation hardening. Strengthening can also be achieved by phase balance. Ultra high strengths steels having mixed microstructures of martensite, bainite and retained austenite are found to have better strength than single phase microstructures [Tomita and Okabayashi, 1983].

2.1.1 Grain size

The relationship between average ferrite grain size, d, and yield stress in steels, σ_y, is described by the Hall-Petch relationship [Gladman, 1997]:

$$\sigma_y = \sigma_0 + k_y d^{-1/2} \quad \ldots (2.1)$$

where σ_0 and k_y are constants.

The constant σ_0, friction stress, represents the stress required to move dislocations along the slip planes in the bcc crystals. This stress is very sensitive to temperature and composition of the steel as seen in Figure 2.1.

k_y is determined from the slope of the line plot between σ_y and $d^{-1/2}$ (Figure 2.1), and has been found to be independent of temperature (Figure 2.1, a), chemical composition of the steel grade (Figure 2.1, b) and strain rate.

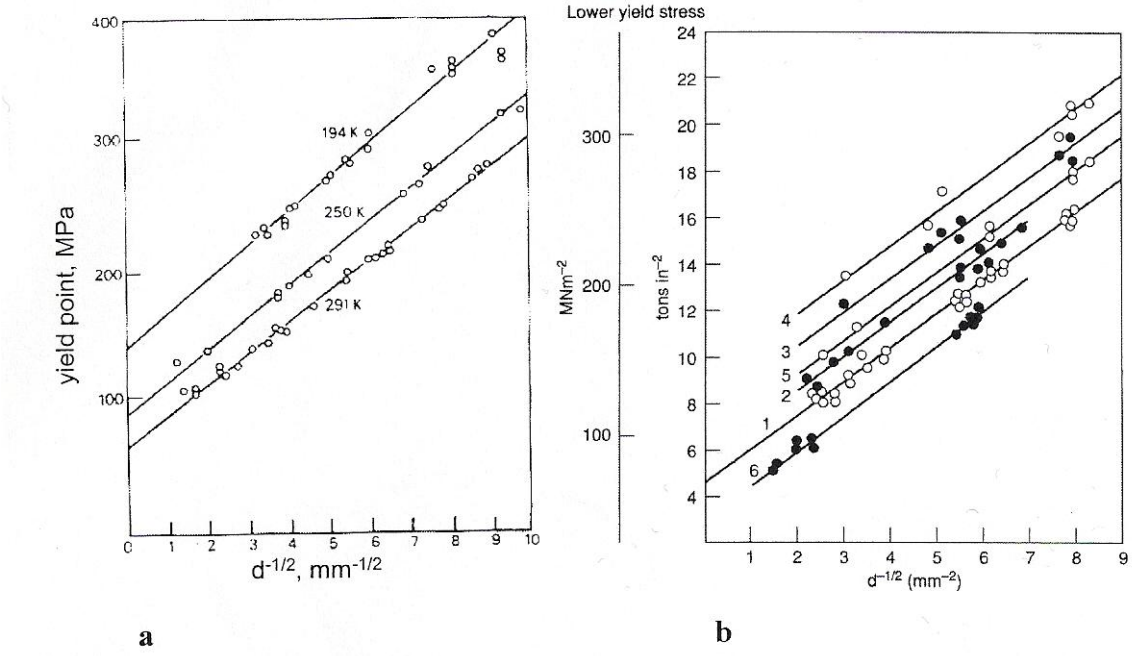

Figure 2.1 Dependence of yield stress on grain size: a) for mild steel at different temperatures [Honeycombe and Bhadeshia, 1995], b) for different solute content of C + N obtained via different quenching procedures [Cracknell and Petch, 1955].

In fine grained material, the length of any slip plane is reduced as grain size decreases so that fewer dislocations pile up at the grain boundary. The stress of the head of the pile-up (Figure 2.2) depends on the number of dislocations in the pile-up; as the number decreases with grain size reduction, a higher external stress to propagate slip into an adjacent grain is required, raising the yield stress (σ_y) [Gladman, 1997].

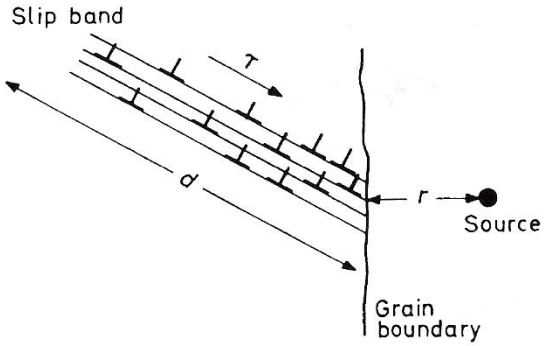

Figure 2.2 Stress intensification arising at the head of the dislocation pile up at a grain boundary [Gladman, 1997].

2.1.2 Solid solution strengthening

Another mechanism of strengthening is alloying with impurity atoms that go either into substitutional or interstitial solid solution causing lattice strains. Due to interactions between dislocations and these impurity atoms that result in lattice strains dislocation movement is restricted. The interstitial solutes carbon and nitrogen are most effective in strengthening the iron by interacting with dislocations and combining with other metallic alloying elements [Honeycombe and Bhadeshia, 1995]. The effects of different alloying elements as solid solution strengtheners are shown in Figure 2.3.

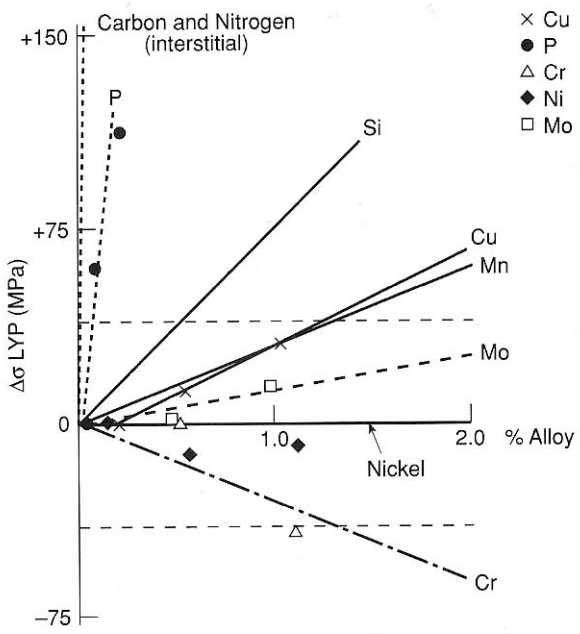

Figure 2.3 Strengthening effects of substitutional solute atoms in iron [Gladman, 1997].

It can be seen that different solutes have different strengthening effects, with the coefficient of phosphorus being much higher than silicon, which in turn is higher than copper, manganese and molybdenum. In addition, nickel shows no solid solution strengthening, whereas chromium shows a negative strengthening effect. The negative strengthening effect of chromium can be explained by the fact that chromium, being a strong nitride former, is removed from solution as chromium nitride [Gladman, 1997]. Strengthening coefficients for various alloying elements are shown in Table 2.1.

Table 2.1 Strengthening coefficients for various solutes [Gladman, 1997]

Solute	C and N (1)	C and N (2)	P	Si	Cu	Mn (1)	Mn (3)	Mo	Ni	Cr
$\Delta\sigma$, MPa	5544	4620	678	83	39	32	31	11	0	-31

(1) [Pickering and Gladman, 1963]
(2) [Cracknell and Petch, 1955]
(3) [Heslop and Petch, 1957]

The strengthening effect increases with an increased difference in atomic size between the solvent atom and the solute atom (Hume-Rothery size effect), as a larger size difference produces a greater disruption of the initial lattice, making slip more difficult [Honeycombe and Bhadeshia, 1995].

Generally solid solution strengthening is used with other mechanisms as it is limited by solubility limits of various solutes and also their effects on hardenability and transformation characteristics.

2.1.3 Precipitation hardening

The matrix can be further strengthened through precipitation or dispersion strengthening due to microalloying elements that precipitate as alloy carbides and / or nitrides. Precipitation strengthening arises from dislocation interactions with fine carbides and nitrides during slip. There are two mechanisms by which dislocations can overcome the precipitates particles: Orowan looping (a by-pass mechanism), Figure 2.4 (a) or by cutting straight through (particle cutting), Figure 2.4 (b).

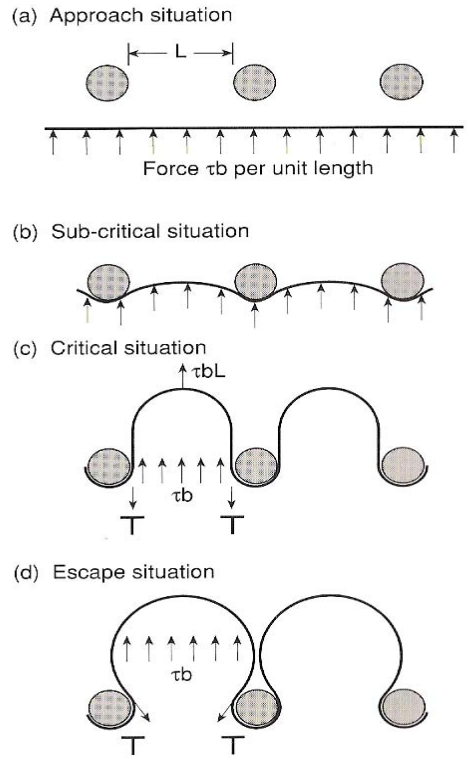

a)

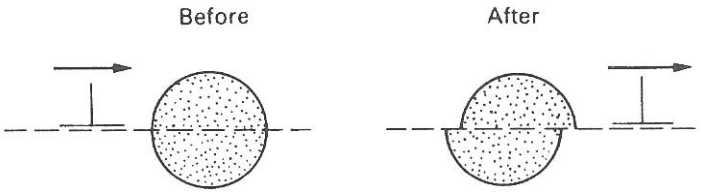

b)

Figure 2.4 Schematic diagram of dislocation interaction with: a) a dislocation meets hard undeformable second phase particles and loops between them (Orowan looping); and b) a soft deformable second phase particles through which dislocation continues to glide (particle cutting) [Gladman, 1997]

When dislocations interact with very fine non-deformable precipitates the dislocations are forced to bow. After extensive bowing of the dislocation, it unpins, and by-passes the particles leaving dislocation (Orowan) loops around the precipitates, Figure 2.4 (a). This is described by Orowan equation [Orowan, 1948], (eqn.2.2), where $\Delta\tau_y$ is

increase in the applied stress (shear) required to free a dislocation of Burgers vector, b, from the pinning particles of spacing, d_p, in a material of shear modulus G.

$$\Delta\tau_y = Gb / d_p \quad \ldots\ldots\ldots (2.2)$$

$$d_p = n_L^{-1} = 4r / 3f \quad \ldots\ldots\ldots (2.3)$$

In order to take into account the particle distribution, the particle spacing, d_p, Equation 2.3, can be substituted into the Orowan equation (Equation 2.2), where n_L is the number of particles of radius r per unit length, and f is the particle volume fraction. For a given volume fraction of particles in a material, d_p increases with increasing r leading to a reduction in dispersion strengthening, Figure 2.5, curve A.

The second mechanism by which dislocations can overcome second phase particles is the particle shearing mechanism, that takes place in the case of soft deformable second phase particles (coherent) which act as weak obstacles to dislocation glide resulting in particle cutting (shearing), Figure 2.4 (b). In this case most strengthening results from coherency strain hardening as the dislocation interacts with the coherency strain around the coherent particle / matrix interface [Gladman, 1997].

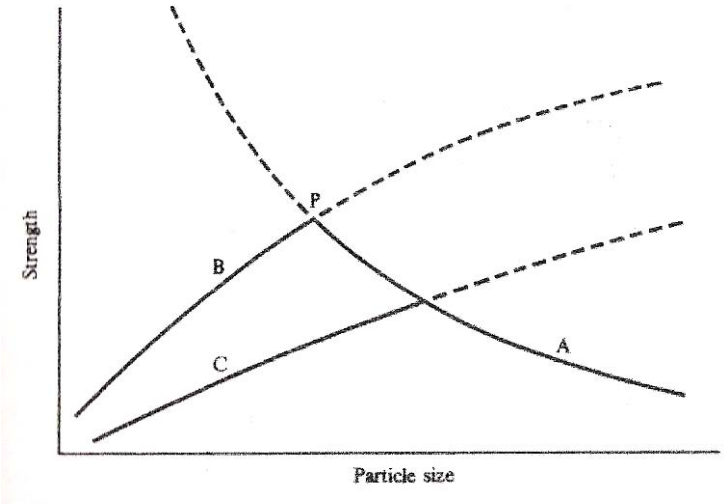

Figure 2.5 Strength as a function of particle size for a typical precipitation-hardened material [Nicholson, 1971].

For small coherent particles the dispersion strengthening increases with increasing particles size, Figure 2.5, curve B. Figure 2.5 shows that there is a critical dispersion at which strengthening is a maximum, point P. The volume fraction of precipitates influences the position of both curves A and B; an increase in volume fraction of precipitates raises the curves and gives higher peak strength, if the particle volume fraction is reduced, both curves A and B are lowered as is the peak strength.

2.1.4 Phase balance

The microstructure of steels often consists of several phases. In plain carbon steels the predominant phase is ferrite with pearlite being the commonest second phase. Apart from these phases in alloyed steels precipitates as carbides, nitrides, carbo-nitrides and intermetallic compounds of alloying elements may be present, they also influencing strength. Increased hardenability and /or cooling may replace pearlite by bainite or martensite, which provide increased strength. Ultra high strength steels consist of mixtures of ferrite, bainite, martensite and / or retained austenite. The effectiveness of the mixed structure is attributed to the fact that lower bainite, which appears in acicular form and partitions prior austenite grains, causes a refinement of the martensitic substructure leading to increased strength [Tomita and Okabayashi, 1984].

2.2 The Development of Precipitates in Steel

2.2.1 Precipitate nucleation

If a liquid metal is cooled below its equilibrium melting temperature (T_m), there is a driving force for solidification (G^S - G^L). In commercial steels solid phases nucleate heterogeneously on the walls of the liquid container and solid impurity particles in the liquid catalyse the nucleation of solid at small undercooking of only ~1 K.

Impurities in contact with the liquid either suspended in the liquid or on the mould walls act as site for nucleation and solid phases nucleate heterogeneously at much lower undercoolings than are necessary for homogeneous nucleation. As nucleation becomes easier less interfacial energy is required to nucleate solid regions, therefore

the energy barrier for nucleation ΔG^* is lowered the snucleation of a new solid phase becomes easer at small undercoolings.

Nucleation in solids is almost always heterogeneous and occurs on non – equilibrium defects as vacancies, dislocations sites, grain boundaries, stacking faults, inclusions and free surfaces [Porter and Easterling, 1992].

In the case of homogeneous nucleation, when no heterogeneous nucleation sites are available large undercoolings are required, as solid nuclei must form homogeneously from the liquid. Solidification will be accompanied by a decrease in free energy, ΔG, and the decrease in free energy provides the driving force for solidification.

The free energies of the liquid and solid at a temperature T ($< T_M$) are:

$G^L = H^L - TS^L$ ……. (2.4)

$G^S = H^S - TS^S$ …….. (2.5)

$\Delta G = \Delta H - \Delta S$, where $\Delta H = H^L - H^S$ is enthalpy difference between liquid and solid, and $\Delta S = S^L - S^S$ is the entropy change.

When the solid forms, an interface is created between it and the liquid. This interface is associated with an interfacial energy (γ).

The creation of small particles of solid leads to a free energy increase, the larger the second phase particle, the greater the increase in interfacial energy. While the driving force promotes phase formation, the need for interfacial energy opposes it; the combined effects of these results in a net energy change that varies with the size of the product formed, Figure 2.6 [Porter and Easterling, 1992].

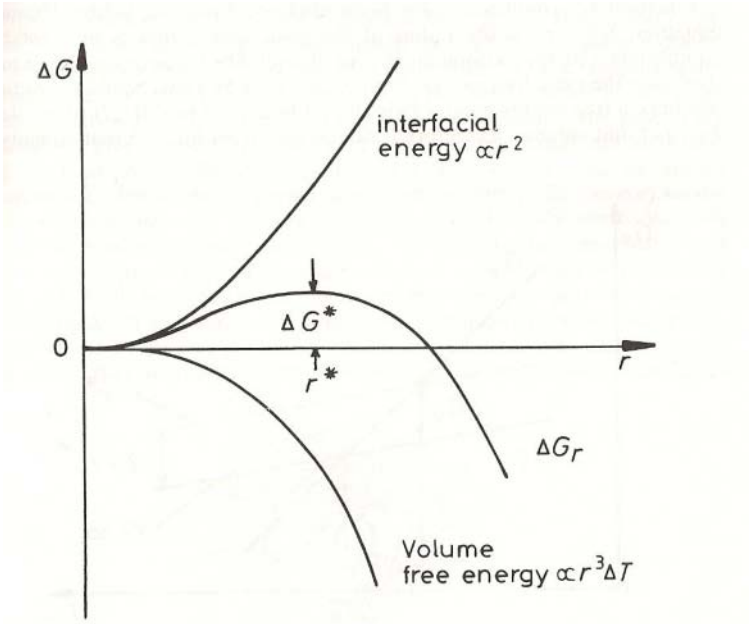

Figure 2.6 The free energy change associated with homogeneous nucleation of a sphere of radius r [Porter and Easterling, 1992].

2.2.2 Particle growth

Once nuclei form within the metastable parent phase, they will grow into the surrounding matrix. During the growth stage, the interface created during nucleation stage migrates into the parent phase. The growth mechanism for precipitates is usually diffusion controlled although the precise type depends on the type of transformation interface and the concentration gradient of solute atoms at the particle / matrix interface.

The particle growth rate is affected by alloy composition and temperature. At small undercoolings, ΔT, the growth rate (V_p) is low due to small supersaturation, ΔX_o, but it is also low at large undercoolings due to low diffusivity. Therefore, a maximum growth rate will occur at some intermediate undercooling ΔT.

At high temperatures near the liquidus temperature, the driving force for particle nucleation will be limited due to low driving force and high ΔG^* value, therefore only particles with the lowest negative ΔH value and ΔG_v are able to nucleate. Once nucleated, the nuclei grow rapidly, due to rapid diffusion of alloying elements,

forming very large particles, which will be coarse and low in number density due to the low nucleation rate and high growth rates at high temperatures.

At low temperatures or at large undercoolings due to the high supersaturation, ΔX_o of carbon and alloy atoms in solid solution and also the slow diffusion will lead to a larger number density of fine particles [Porter and Easterling, 1992].

Nucleation of bainite takes place at austenite grain boundaries or intragranularly at nonmetallic inclusions [Bhadeshia, 1992].

2.2.3 Particle coarsening

Microalloyed steels heated into single phase austenite phase, but below the solvus temperature of particles present will cause Ostwald ripening of the particles.

Ostwald ripening can be defined as a selective growth of same second phase particles, usually the larger particles, at the expense of the other particles of the same phase, usually the smaller particles, which will decrease in size until they disappear completely. In the Ostwald ripening process, by coarsening of the particles the total interfacial energy between matrix and precipitate is reduced.

The Gibbs–Thomson equation (equation 2.6) relates the local solubility at the particle – matrix interface with the particle size.

$$\ln (S_r / S) = 2\Omega\sigma / RTr \quad \ldots\ldots\ldots\ldots\ldots\ldots (2.6)$$

where S_r is the solute content in equilibrium with a particle of radius r, S is the true equilibrium solubility (flat interface), Ω is the molar volume of the precipitate, γ is the interfacial energy between particle and matrix, R is the gas constant and T is the absolute temperature, K.

Equation (2.6) shows that a small particle will give a high level of solute in the matrix near the particle surface, whereas a larger particle will give a lower level of solute near the particle. The level of solute in the matrix will be intermediate between the equilibrium levels for the smallest and the largest particles, and diffusion of the solute will occur from the high concentration regions near the small particles towards the low concentration regions near the large particles. This way the local equilibrium is disturbed and some dissolution of the smaller particle will occur to re-establish the equilibrium solute content resulting in a decrease of the particle size and an increase

in the local equilibrium content. The repeated diffusion and dissolution will result in disappearance of the small particles.

The diffusion of solute to the low concentration regions near the large particles will result in local supersaturation followed by precipitation and particle growth and this way the Gibbs –Thomson equilibrium level is re-established [Gladman, 1997].

2.3 Matrix transformation behaviour in steels

2.3.1 Martensite

When a steel is cooled rapidly enough from the austenitic field insufficient time is allowed for carbon to diffuse out of solution and the steel transforms to martensite, which is a supersaturated solid solution of carbon trapped in a body centred tetragonal structure. The martensitic reaction is a diffusionless transformation that occurs athermally, therefore, the transformation depends only on the decrease in temperature and is independent of time. The reaction begins at a martensitic start temperature, M_s, that can be ~500 ºC in low carbon steels, but increasing carbon content decreases the M_s temperature. Martensitic nucleation takes place heterogeneously on pre – existing embryos, which are present in the austenite at temperatures above M_s and which become activated at temperatures below M_s [Bhadeshia, 1992]. The embryos have a semi coherent dislocation interface with the austenite, growing taking place by nucleation of new dislocations loops which join the interface and extend it [Honeycombe and Bhadeshia, 1995].

The driving force for the nucleation of martensite at the M_s is:

$\Delta G^{\gamma\rightarrow\alpha'} = \Delta H^{\gamma\rightarrow\alpha'} (T_0 - M_s) / T_0$, where T_0 is the temperature at which fcc and bcc / bct phases of the same composition possess the same free energy.

Below the M_f temperature (martensite finish) further cooling does not increase the amount of martensite [Porter and Easterling, 1992]. At this temperature all the austenite should have transformed to martensite but in practice some retained austenite can be left even below M_f.

Most alloying elements which enter into solid solution in austenite lower the M_s temperature, but the interstitial solutes carbon and nitrogen have a much larger effect than the substitutional alloying elements, with 1 wt % C lowering the M_s by over 300 ºC [Honeycombe and Bhadeshia, 1995]. The relative effects of carbon and other alloying elements can be expressed using a number of empirical relationship covering different composition ranges e.g. equation (2.7) [Steven & Haynes, 1956].

$$M_s\ (^oC) = 561 - 474\ (\%\ C) - 33\ (\%\ Mn) - 17\ (\%\ Ni) - 17\ (\%\ Cr) - 21\ (\%\ Mo) \quad \ldots\ldots\ldots (2.7)$$

The most important property of martensite is its potential of very great hardness. The origin of high strength of martensite is due to several strengthening mechanisms: interstitial solid solution strengthening from carbon, which results in the tetragonality of martensite as the major strengthening factor, grain size, and precipitation hardening (for tempered martensite).

2.3.2 Bainite

Bainite is produced when austenite decomposes at temperatures above those for martensitic formation but below those for pearlite formation through either isothermal transformation or continuous cooling.

Bainite is a mixture of ferrite and carbide as for pearlite but is microstructurally different from it and characterised by its own 'C' curve on the TTT diagram. In plain carbon steels this curve overlaps with the pearlite curve so that, at temperatures around 500 ºC, pearlite and bainite form competitively, whereas in alloyed steels the two 'C' curves are separated [Porter and Easterling, 1992].

The bainite reaction takes place isothermally and it starts with an incubation period during which no transformation is detected, followed by an increasing rate of transformation to a maximum then slowing down gradually. The microstructure of bainite depends mainly on the temperature at which it forms. Transformation begins at a bainite start (B_s) time and ends at a bainite finish time (B_f) time. As the transformation temperature is lowered the type of bainite changes: the bainite that forms at high temperature (350-550 ºC) just below the nose of the curve is coarser, upper bainite, whereas bainite that forms at lower temperatures of the transformation range (350-250 ºC) is finer, lower bainite, and resembles martensite.

Upper bainite consists of needles or laths of ferrite with cementite precipitates between the laths, Figure 2.7. The growth of upper bainite is diffusion controlled and is governed by the rate of carbon diffusion in austenite away from austenite / ferrite interface [Radcliffe et al., 1963]. The amount of cementite precipitated depends on the carbon concentration of the alloy; therefore, when the alloy carbon concentration is high, the laths are separated by continuous layers of cementite. Low concentrations of carbon lead to formation of discontinuous layers of small particles of cementite. The formation of cementite can be suppressed when sufficient quantities of alloying elements (Si or Al) are added to the steel, resulting in an upper bainite that consists of just bainitic ferrite and carbon-enriched retained austenite [Honeycombe and Bhadeshia, 1995]. Subsequent cooling transforms retained austenite to deformation-induced martensite [Horn and Richie, 1978, and Bhadeshia and Edmonds, 1983].

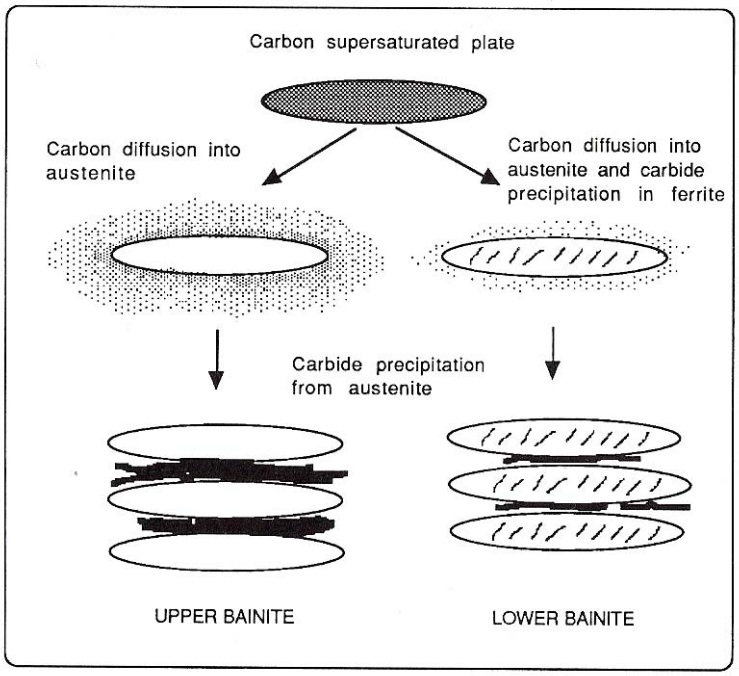

Figure 2.7 Schematic representation of the transition from upper to lower bainite [Bhadeshia, 1992].

The transition temperature from upper to lower bainite varies with carbon content, [Oka and Okamoto, 1986] and the microstructure of bainite changes from laths into plates with the carbide dispersion becoming finer, Figure 2.7. At the temperatures where lower bainite forms, carbon diffusion is slow and carbides precipitate in the ferrite with an orientation relationship being aligned to the plane of ferrite plate at approximately the same angle [Porter and Easterling, 1992].

By altering the isothermal holding temperature and time the amount of austenite transformed to bainite can be controlled, affecting also the amount and carbon content of retained austenite [Sandvik and Nevalainen, 1981].

2.3.3 Tempering characteristics

The purpose of tempering is to relieve residual stresses left in the steel due to the formation of martensite and to improve ductility and toughness. Martensite, which is a supersaturated solid solution of carbon in iron, during tempering rejects carbon in the form of finely divided carbide phases and transforms to tempered martensite, consisting of a fine dispersion of carbides in an α iron matrix. Tempering is accomplished by heating the as-quenched sample to a temperature below the eutectoid temperature, so that the driving force for precipitation is strong. Tempering takes place in four distinct but overlapping stages:

Stage 1, up to 250 ºC with precipitation of ε-iron carbide and partial loss of tetragonality of martensite; Stage 2, between 200-300 ºC with decomposition of retained austenite; Stage 3, between 200 and 350 ºC during which ε-iron is replaced by cementite and martensite loses its tetragonality; Stage 4, above 350 ºC- cementite coarsens and spheroidises.

Alloying elements reduce the coarsening of cementite in the temperature range 400-700 ºC due to the formation of alloy carbides in the temperature range 500-600 ºC, because below this temperature the diffusion of alloying elements is slower [Honeycombe and Bhadeshia, 1995].

2.4 Composition of 300M

AISI 300M is a commercial ultra-high strength alloy low alloy steel, which has been employed in critical structural components for aerospace vehicles [Tomita, 1991].

The composition of 300M is specified in the range (wt %) of C 0.38 – 0.43, Mn 0.6 - 0.8, Mo 0.4, Ni1.65 -2, Cr 0.7 -09 [Metals handbook, 1990], containing other micro alloying additions (< 0.1 wt %) of elements such as Ti, V and Al. As a medium carbon steel it is heat treatable to high strength by quenching and tempering treatments.

The 300M steel was introduced as a higher strength replacement for 4340 steel, which can be heat treated to high strength (1.5 GPa yield) and toughness (63 MPa √m).
This alloy has been modified (300M) to give higher strength levels (1.75 GPa yield) for similar toughness (65 MPa √m) by increasing the level of Mo (from 0.2 - 0.3 up to 0.4 wt %) which provides greater precipitate strengthening and hardenability and from raising Si level (from 0.3 to 1.6 wt %) as well as a small amount of vanadium.

The silicon addition allows the steel to be hardened within a tempering temperature region outside the brittle temper region, as silicon retards the precipitation of cementite from the residual austenite during bainitic transformation.
The vanadium alloying tends to form fine vanadium-rich carbo-nitrides during tempering contributing to increased precipitation hardening [Tomita and Okawa, 1993].
The additions of Mn, Ni and Mo, which are austenite stabilisers, and Cr, which is a strong carbide former, increase the hardenability of the steel.

The alloy modifications, together with vacuum induction melting give the steel a higher strength than that of 4340 steel.

2.5 High Strength, High Toughness alloys

Grain refinement, precipitation hardening, and phase balance provide the main strengthening mechanisms in high strength, high toughness alloys.
Mechanical properties of high strength, high toughness alloys are strongly influenced by the changes in alloy composition and processing including final heat treatment that affect the final grain size, particle distribution and phase transformation.

2.5.1 Role of inclusions and fine particle dispersions on strength and toughness

In steels the primary particles are inclusions which can be sulphide, oxide and nitride particles. Inclusions tend to be larger than other second phase particles, ranging in diameter from 0.1-10 μm or more.
The secondary particles include the fine carbides, nitrides and carbo-nitrides inherited from the austenitising temperatures and particles precipitated on tempering. Secondary particles directly influence fracture if they nucleate voids, and they can indirectly influence toughness by pinning the austenite grain boundaries during austenitising and so influencing prior austenite grain size [Garrison and Wojcieszynski, 2007].
Toughness can be improved by controlling the non-metallic inclusion amount, size, shape, chemical composition and location [Leslie, 1983]. In order to reduce the effect of MnS inclusions, different technologies have been employed: desulphurisation, calcium treatments [Tomita, 1999] and decreased hot rolling reduction [Tomita, 1988].
With a decrease in the sulphur content through desulphurisation, the volume fraction of MnS has been reduced significantly, but in case of calcium treatment, for steel with a commercial sulphur level it was not very effective in modifying inclusion shape, whereas the calcium treatment of desulphurised steel dramatically modified the stringer-type of MnS inclusions to a more particulate type [Tomita, 1995].
Decreasing the hot–rolling reduction from 98 to 80 % for the commercial AISI 4340 steel modified the shape of sulphide inclusions from stringers (average aspect ratio = 17.5) to ellipses (average aspect ratio = 3.8) and improved K_{1C} values in the longitudinal testing orientation by about 20 MPa $m^{1/2}$ at similar strength levels. The

decrease in the hot-rolling reduction also increased the K_{1C} values in the transverse testing orientation by about 17 MPa $m^{1/2}$ at increased ductility and Charpy impact energy levels [Tomita, 1988].

Coarse TiN particles, typically 1-6 μm, have been shown to impair toughness, by promoting cleavage crack initiation [Linaza et al., 1995; Zhang et al., 1999]. TiN particles, because of their high thermodynamic stability are often used as grain refiners, but the content of Ti and N as well as process parameters need to be controlled as TiN particles can form in the melt or in the semi-solid regions where they grow to large sizes [Balart *et al.*, 2001], with particle size proving more important than number density [Li and Zhang, 1989]. The coarse TiN particles are not affected by processing in the solid state [Leap and Wingert, 1999].

In highly loaded situations, properties can be dependent on the spatial distributions of the TiN and MnS, especially for higher strain rate and / or lower temperature testing when any cracks formed by particle decohension or fracture are not blunted out, [Zhang *et al.*, 2001].

In order to achieve optimum toughness in HSLA steel a fine dispersion of precipitates that are thermodynamically stable at high temperatures to maintain a fine grain size; and a low density of coarse inclusions are required [Gore *et al.*, 1987]. The precipitation strengthening particles in quenched and tempered HSLA and medium carbon steels are mainly alloy carbo-nitrides.

2.5.2 Phase effects on strength and toughness

HSLA steels having a mixed structure of martensitic and non-martensitic decomposition products have been found to have better strength and toughness than single phase microstructures of low temperature products, Figure 2.8 (a) [Tomita and Okabayashi, 1983; 1985; 1987; 1988]. Tomita and Okabayashi [1985] studied the effect of bainite on the mechanical properties of a 0.4 wt % C high strength steel (AISI 4340) having a mixed structure of martensite and bainite, showing that the presence of 25 vol % lower bainite gave maximum strengthening, Figure 2.8 (b), and

further increase in lower bainite volume fraction gradually reduced strength to levels corresponding to a single phase lower bainite.

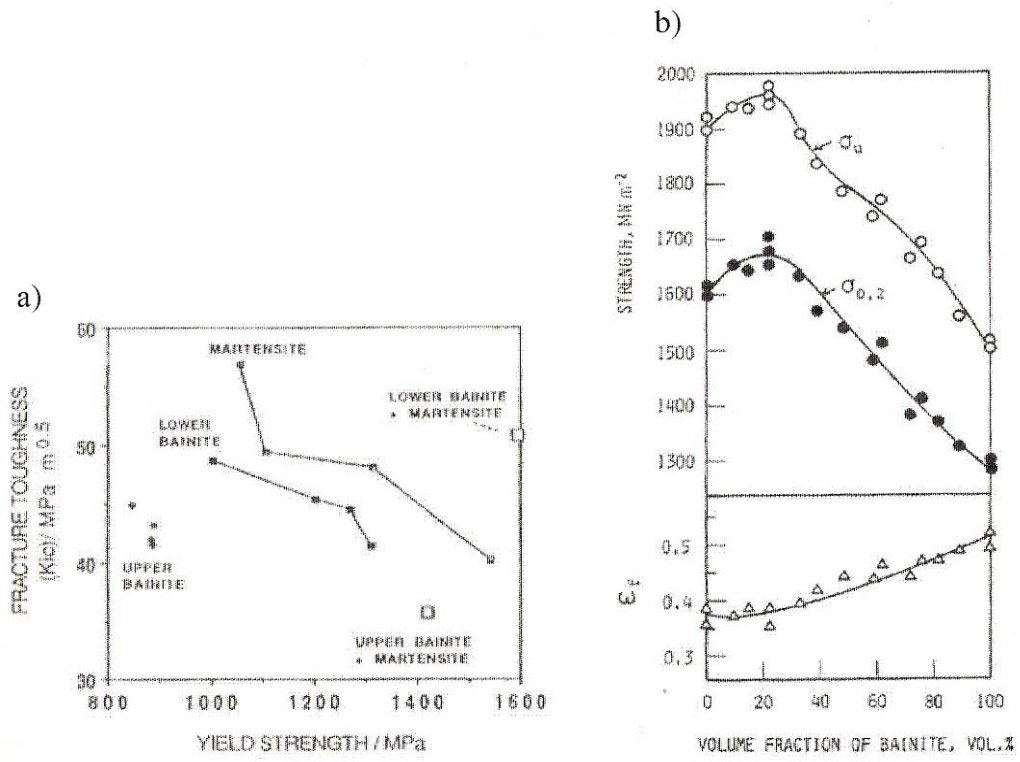

Figure 2.8. Strength and toughness of 0.4 wt % C high strength steel tempered at 200 ºC showing; a) effects of phase balance on K_{IC}; and b) effect of volume fraction of lower bainite on strength $\sigma_{0.2}$ and σ_U (UTS) and fracture ductility ε_f (elongation of failure) [Tomita, 1991].

Tempering the mixed structure at temperatures > 400 ºC resulted in lower strengths regardless of the volume fraction of lower bainite. With increasing tempering temperature the difference in strength of martensite and bainite reduced and after tempering at 600 ºC, the strength of martensite was approximately equal to that of lower bainite [Tomita and Okabayashi, 1985]. As martensite has more carbon in solution and therefore a greater response to tempering than bainitic ferrite, the difference in strength between martensite and lower bainite is reduced.

When the steel has a mixed structure of martensite and bainite, the shape and distribution of the second phase bainite has a significant effect on the K_{1C} value.

Lower bainite, which appears in acicular form and partitions prior austenite grains of the parent martensite dramatically improves toughness in association with tempered martensite, whereas, when upper bainite, which appears as more equiaxed regions that fill prior austenite grains of the parent martensite, significantly lowers $K_{1C.}$ AISI 4340 steel having 25 % lower bainite, quantified by optical microscopy, in association with tempered martensite improves the K_{1C} value by 11 MPa $m^{1/2}$. while a steel having a mixed structure of martensite and 25 % upper bainite compared to martensitic steel decreased the K_{1C} by about 5 MPa $m^{1/2}$ [Tomita, 1988].

Tomita has shown that in AISI 4340 type steel, the strength of lower bainite is enhanced by the constraint provided to its deformation by the surrounding martensite. This restraint also enables the bainite to deform in association with the martensite allowing the crack arresting and stress relieving effects to improve the fracture ductility and toughness. It has been also shown that the degree of plastic restraining on lower bainite depends on the martensite carbon content, higher carbon martensite giving increased plastic restraining of the bainite [Tomita, 1991].

Tomita and Okabayashi [1985] concluded that the mechanical properties of high strength steels having a mixed structure of martensite and bainite are affected more by size, shape, and distribution of bainite rather than the difference in martensite and bainite strength or by the type of mixed bainite present.

2.5.3 Effect of temperature austenitisation on second phase particles in 300M

Studying the influence of different austenitisation temperatures on the microstructure of 300M steel, Youngblood and Raghavan [1977] showed that austenitisation at 870 °C for 1h resulted in many undissolved particles that varied in size with diameters ranging from 100 to 200 μm and having a fcc structure.

In order to determine the lowest austenitisation temperature which would dissolve the second phase particles, the study involved austenitising at various temperatures, between 870 and 980 °C and times from 1 to 8 hours.

Transmission Electron microscopy revealed that extended holding times up to 8 hours at 870 °C did not dissolve the particles, nor did a slight increase in temperature to 899 °C for 1h. The size and number density, N_d, of these particles were not reported.

Further increase in the austenitisation temperature to 927 °C with 1h holding time eliminated most of the precipitates, and after 1h at 982 °C, second phase particles appeared to be completely dissolved.

Tempering in the range 204 - 316 °C showed an increase in toughness with increasing austenitisation temperature, with the most pronounced improvement occurring concurrently with the dissolution of second phase particles, i.e. at high austenitisation temperature, Figure 2.9 [Youngblood and Raghavan, 1977].

Ritchie and Horn [1978] showed that for AISI 4340, an improvement in fracture toughness resulted from the dissolution of void-initiating particles at high austenitisation temperatures. Austenitisation at increasing temperatures: 870 °C, 1000 °C, 1100 °C and 1200 °C resulted in increased particle spacing due to dissolution of carbides and led to improved fracture toughness. This conclusion was reached by analysing the dimple size and spacing observed on fracture surfaces by scanning electron microscopy.

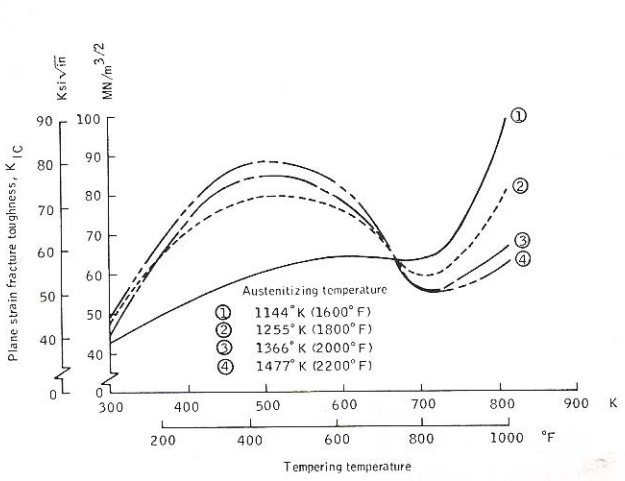

Figure 2.9 Effect of tempering temperatures on the plain-strain fracture toughness of 300M steel austenitised at different temperatures in the range 1144 -1477 K [Youngblood and Raghavan, 1977].

Previous studies quantified the microstructures and particle distributions as a function of composition variations (mainly Ti) and processing parameters. The objectives of this study are to determine the effects of heating to and cooling from different austenitisation temperatures on the resulting microstructures and fine particle (<600 nm) distributions, the results being related to mechanichal properties hardness and toughness.

CHAPTER 3
Experimental Approach

3.1 Material

Two casts representing variations of commercial-aircraft quality 300M steel, which were double melted (electric arc furnace melted, vacuum arc remelted and degassed), from two sources were used in this project. Material from source 1 (steel C) was hot rolled, whereas material from source 2 (steel D) was forged before heat treatment. The major alloying element variations are listed in Table 3.1.

The processing history of the steel from source 1 is: the cast ingots were allowed to cool to room temperature after solidification then ground in order to remove the outermost layer, re-heated to the 1250 ^{o}C ingot soak temperature, then hot rolled to either 100 mm or 220 mm (side length) square bar, followed by a pit cool to room temperature. The rolled bars were then softened by an intercritical anneal at 750 ^{o}C. For the forged steel, the processing route is slightly different from the previous one as it was forged rather than rolled and received a softening heat treatment (details unknown).

Table 3.1 Major alloying element variations for the 300M samples used in this study

Composition (all elements in wt %)

Steel	C	Mn	S	N	Ti	Al	Mo
C	0.42	0.80	0.002	0.004	0.006	0.023	0.39
D	0.41	0.77	0.0008	0.002	0.0032	0.041	0.41

C = 300M from source 1

D = 300M from source 2

3.2 Heat Treatment

Heat treatments were carried out using a Carbolite electric furnace in order to investigate the change in particle distributions (size and volume fraction). For the first heat treatment (SHT) two samples were austenitised at 925 ^{o}C for 1h, air cooled then one of the samples was used for the second reheat to 870 ^{o}C for 1h and oil quenched. Samples were placed on ceramic tiles with a thermocouple between them, timing commenced once they reached the required temperature, which was monitored by the thermocouple. The same procedure was used for subsequent trial heat treatments, Table 3.2:

Table 3.2 Trial heat treatment details

1.	
Temperature: 925 ºC	Holding time
Water quenched (WQ)	1h
Water quenched	2h
Water quenched	4h
2.	
Temperature: 1025 ºC	Holding time
Water quenched	2h
Air cooled (AC)	2h
3.	
Temperature: 870 ºC after 1025 ºC AC	Holding time
Oil quenched (OQ)	1h
4.	
Temperature: 300 ºC	Holding time
Air cooled	2h
Air cooled	2h

3.3 Image Analysis and optical microscopy

Transverse sections (steel D), comprising of a 2 mm thick slice, were mounted in conducting Bakelite, ground and polished to a final 0.25 µm alumina paste finish then etched in 2% nital. The specimens were imaged using a Leica DMRX microscope and analysed using KS 300 software in order to quantify the coarse optically resolvable TiN particle size and number density distribution. Measurements were made across the thickness, totalling an area of approximately 51.7 mm^2 for each of the three conditions: initial condition: 925 °C 1h AC and 870 °C 1h OQ. The coarse TiN particles were measured as side length and side breadth.

For the determination of upper bainite percentage an area of 0.84 mm^2 was imaged for each heat treatment condition. The area fraction of upper bainite was measured using the interactive method from digital images acquired from etched optical specimens.

3.4 Scanning electron microscopy (SEM)

SEM was carried out on the JEOL 6060 and Philips XL-30 with low vacuum capability. Fine particles were imaged for all the heat treatment conditions and characterised in terms of size, number density distribution and volume fraction. Thirty continuous fields of views were taken from a total area of 12348.68 μm^2 at 40 µm intervals, for all the conditions. To determine the chemical composition of the particles (TiN, MnS, Mo-rich particles), polished and etched samples were examined using JEOL 6060 equipped with Oxford Inca energy dispersive X-ray spectroscopy (EDS) and Philips XL-30 equipped with Oxford Isis EDS with an operating voltage of 20 kV and a working distance of 10 mm.

3.4.1 Fractography

The K_{1C} specimen fracture surfaces were examined on the Philips XL-30 SEM. The initiation zone was imaged at a magnification of 500x in order to identify failure mode and thirty continuous fields of views were taken for the two conditions.

In order to examine the ductile areas, thirty continuous fields of views were taken at a higher magnification of 5000x, in two areas: a) initiation zone and b) beyond the initiation zone, in the first half of the fracture zone. Dimples were measured using the interactive method from SEM images.

3.5 Thermodynamic Calculations

Version Q of the Thermo-Calc (T-C) software optimisation package from the Royal Institute of Technology, Stockholm was used to predict phase balance, nature and composition of phases under equilibrium conditions, over the temperature range 1300-600 ^{o}C. The parameters entered were temperature, atmospheric pressure and weight percent of elements contained both in the alloy and database: Fe, C, Si, Mo, P, S, Cr, Ni, Al, N, Nb, Ti and V. T-C was used to predict phase compositions and weight fraction of the precipitates present at equilibrium.

3.6 Mechanical Testing

3.6.1 Hardness Testing

An Indentec Vickers macrohardness tester was used for macrohardness measurements (H_v) for all the conditions. The average H_v was based on six indents made near the centre on specimens at room temperature using a 10 kg load.

3.6.2 Fracture toughness testing

Samples from steel C were machined into standard compact tension (C-T) specimens, 12.5 mm thick (Figure 3.1), as recommended in BS 7448, so that the rolling direction was parallel to the notch. They were heat treated according to the schedules specified in the Table 3.3.

Fatigue precracking was carried out on a Amsler machine and fracture toughness testing was carried out on a Instron 8862 screw driven machine at a constant displacement rate of 0.5 mm / min.

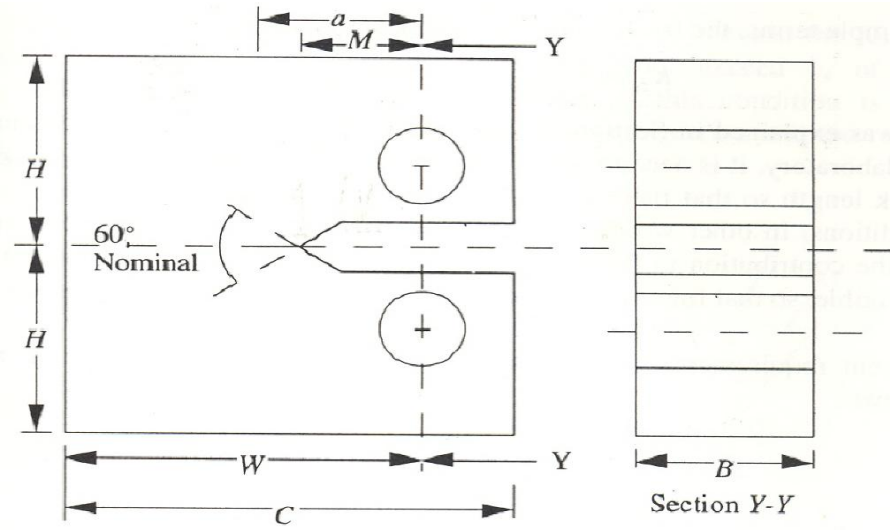

Net Width	$= W$
Total width C	$= 1.25W$
Thickness B	$= 0.5W$
Half height H	$= 0.6W$
Hole diameter	$= 0.25W$
Effective notch length M	$= 0.25W$ to $0.40W$
Effective crack length a	$= 0.45W$ to $0.55W$

Dimensions in mm.

Fig.3.1 Shape and dimensions (mm) of (C-T) specimens (Knott and Withey, 1998)

Table 3.3 Heat treatment schedule for fracture toughness testing

1.	
Temperature: 925 ºC	Holding time
Air cooled	1h
Temperature: 870 ºC	Holding time
Oil quenched	1h
Temperature: 300 ºC	Holding time
Air cooled	2h
Air cooled	2h
2.	
Temperature: 1025 ºC	Holding time
Air cooled	2h
Temperature: 870 ºC	Holding time
Oil quenched	1h
Temperature: 300 ºC	Holding time
Air cooled	2h
Air cooled	2h

CHAPTER 4

Results and Discussion

4.1 Characterisation of coarse particles (TiN and MnS)

TiN and MnS in this alloy have high thermodynamic stability and are expected to form at elevated temperatures retaining their size, shape and distribution on subsequent heat treatment. Coarse particles observed in the steel in this study were identified as being based on TiN and MnS. The coarse TiN particles, Figure 1(a) and (b), are typically angular in shape, and range in size from 1 - 20 µm in side length, consistent with the size of TiN forming in the liquid and during initial stages of solidification in Ti-containing steels [Zhang *et al.*, 1999; Li & Zhang, 1989].

At high temperatures > 1200 ºC, coarse TiN can act as favourable nucleation sites for MnS [Balart *et al.*, 2000], Figure 4.1(c) and (d).

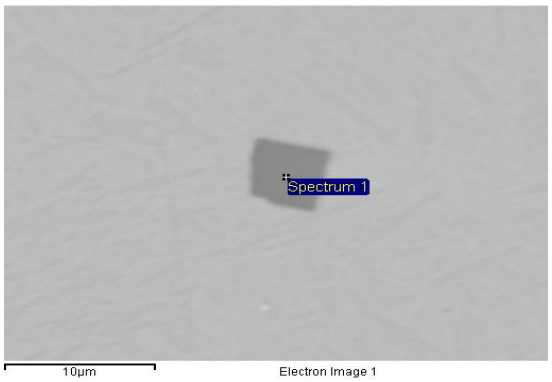

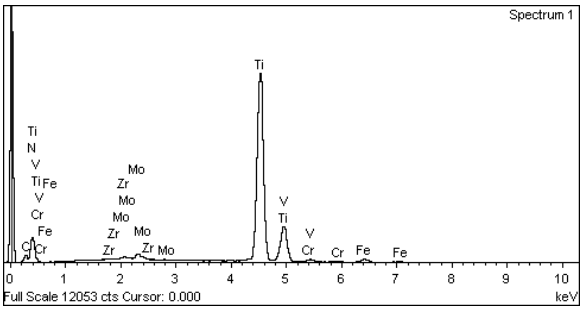

a) b)

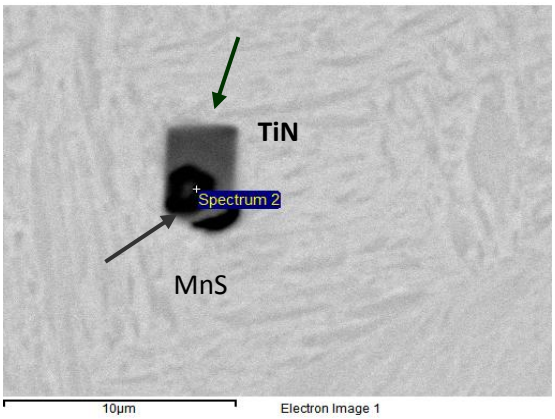

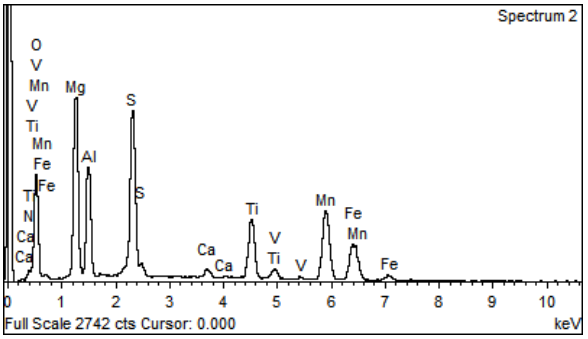

c) d)

Figure 4.1 a) Angular coarse TiN particle; b) EDS spectrum from TiN particle; c) TiN particle with MnS inclusion attached; d) EDS spectrum from the attached MnS.

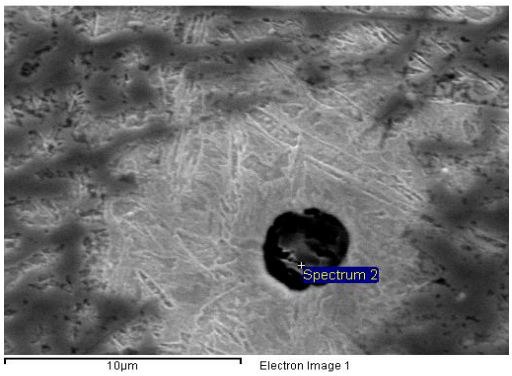

a)

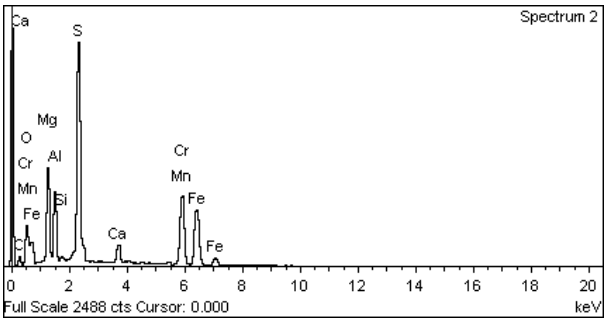

b)

Figure 4.2 a) Spherical MnS particle b)EDS spectrum from MnS indicating the presence of Ca and Al.

Manganese additions to low – medium carbon steels promotes the formation of manganese sulphide and prevents formation of the less stable lower melting point iron sulphides [Gladman, 1997]. As the samples have been sectioned normal to the forging direction the steel appears to contain spherical sulphides, Figure 4.2 (a) and (b), rather than elongated manganese sulphides [Gladman, 1977]. This, however, is merely a sectioning effect. EDS analysis identified the presence of Ca and Al in the MnS particles, Figure 4.2 (b) which were taken to be CaO and Al_2O_3 from steel deoxidation reactions. Calcium may have been added to the forged steel as a sulphide shape controlling addition and as a refiner of TiN particle size [Berry, 2001].

Table 4.1 Summary of results for TiN particles: number, size, number density (N_d) and volume fraction (V_f) of TiN measured and predicted.

Condition	Number of particles	Size range (µm) longest side length	N_d (TiN) per cm^2	Measured V_f (TiN)	Predicted V_f (TiN)
Initial condition (IC)	53	1.6 - 20	102	3.25×10^{-5}	
925 ºC AC	61	1.6 - 11.6	117	4.06×10^{-5}	1.4×10^{-4}
870 ºC OQ	56	1.6 - 13.3	108	2.98×10^{-5}	

Figure 4.3 shows the number density N_d of TiN for the three conditions, indicating a similar distribution for the coarse TiN particles. In addition, V_f follows the same trend, Table 4.1, indicating that the TiN particles were not affected by subsequent heat treatments. The sizes and distribution of TiN for AC and OQ states are similar; this indicates that the V_f values are prone to wide scatter i.e. no differences between 3 and 4 x 10^{-5}, Table 4.1. The distribution for IC (initial condition which is the prior condition to the heat treatments), however, appears to be smoother with fewer 5 - 10 µm (15 particles compared to 30 particles for AC and OQ) and more > 15 µm (1 particle) size particles. The V_f value is not significantly different and neither is N_d, suggesting that the differences for 5 - 10 µm and > 15 µm size ranges could be a measure of sampling errors inherent in such clean melted steels.

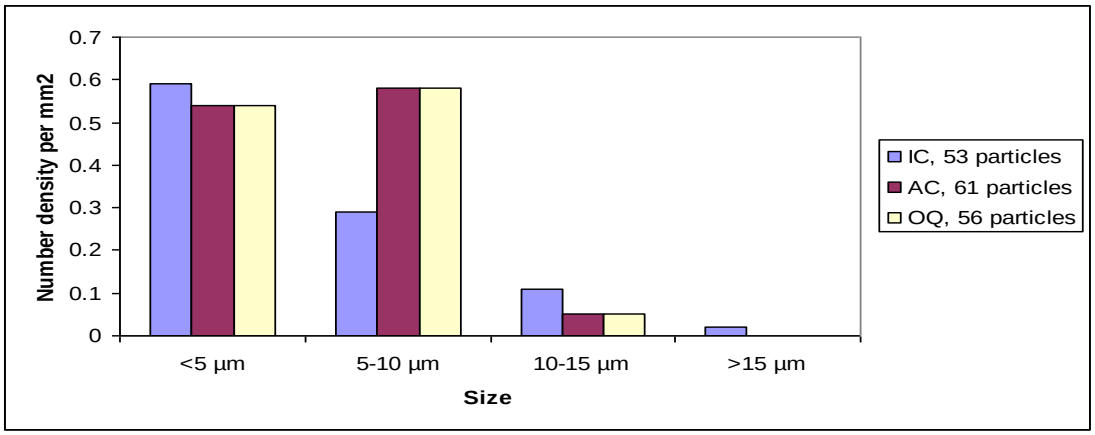

Figure 4.3 Histogram of number density of TiN particle for IC, AC and OQ conditions.

Thermo-Calc predictions of the V_f of TiN at 925 ºC show a higher value than the measured one, $1.4x10^{-4}$ compared to 4.06×10^{-5}, Table 4.1, because T-C predictions are related to equilibrium conditions.

The predicted V_f of TiN was calculated using the predicted "Mass" of the carbo–nitride at 925 ºC from the T-C output data, which was then divided by the density of TiN (5.4 g/cm3) [Chen et al., 1999] in order to get the volume of the carbo-nitride, then the volume of carbo-nitride was divided by the total volume of the system derived from T-C in order to get the volume fraction.

Figure 4.4 (a) shows that the carbide started forming at 1300 ºC and reaches maximum weight at 800 ºC; from 1300 ºC up to 925 ºC the carbide is rich in Ti (5) and from 925 °C downwards the carbide becomes rich in Mo (2), Figure 4.4 (b).

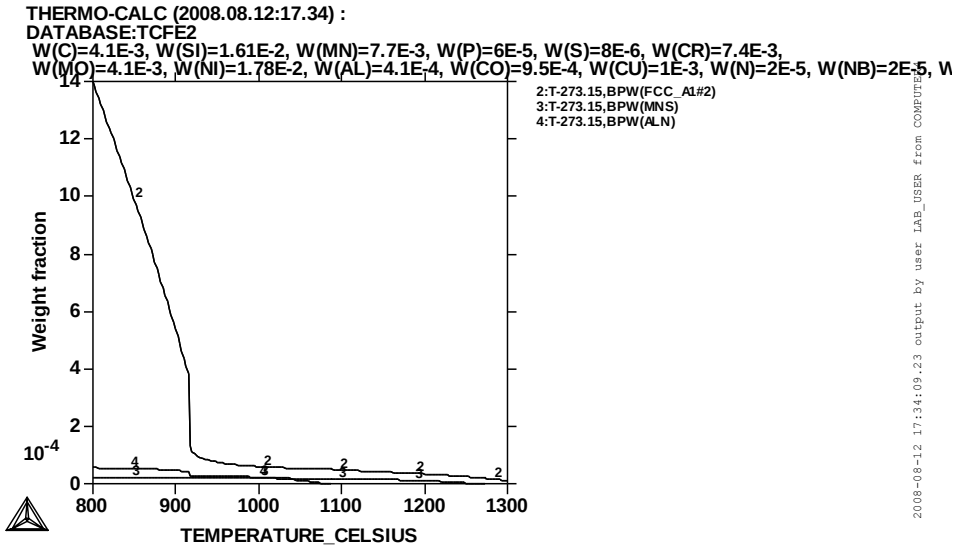

a)

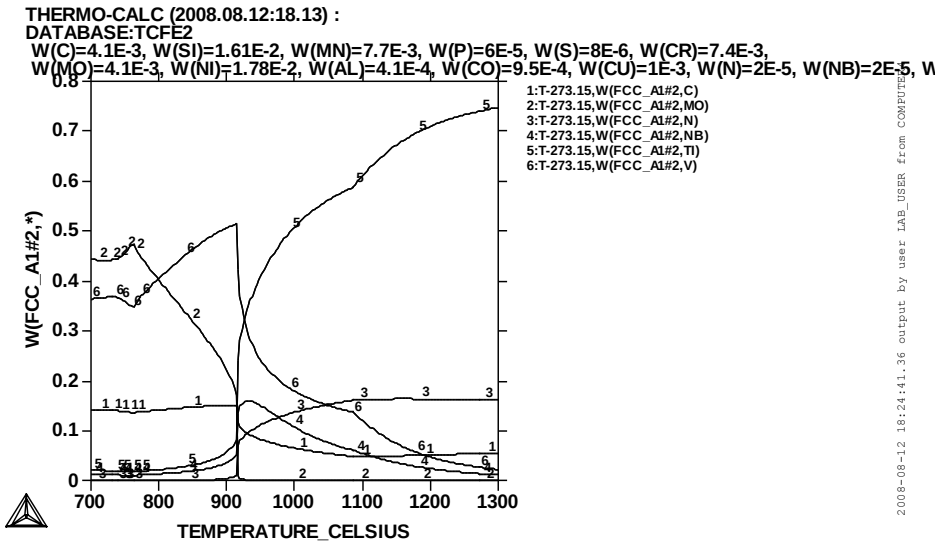

b)

Figure 4.4 a) Variation of weight fraction of carbide with temperature and b) elemental variation within the complex carbide with temperature.

4.2 Characterisation of fine (< 600 nm) particles

The composition of 300M steel contains a number of carbo-nitride formers and so would be expected to form a variety of precipitates over a range of temperatures: coarse TiN and MnS at high temperature and finer precipitates in the solid state at lower temperatures. Figure 4.5 (a) and (b) indicates the presence of fine rounded particles which were identified by SEM-EDS to be Mo-rich. Mo-rich particles were quantified (size, number density and volume fraction) for eight conditions. Six size diameter ranges were chosen: <100 nm, 100-200 nm, 200-300 nm, 300-400 nm, 400-500 nm and 500-600 nm, Section 3.4, as no particles larger than 600 nm were observed.

Table 4.2 summarises the overall particle number densities (N_d) and volume fractions (V_f) for the conditions studied.

a)

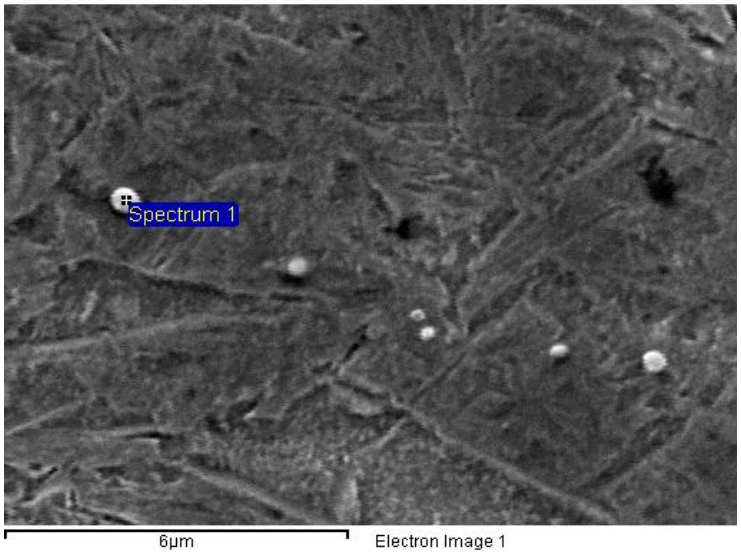

b)

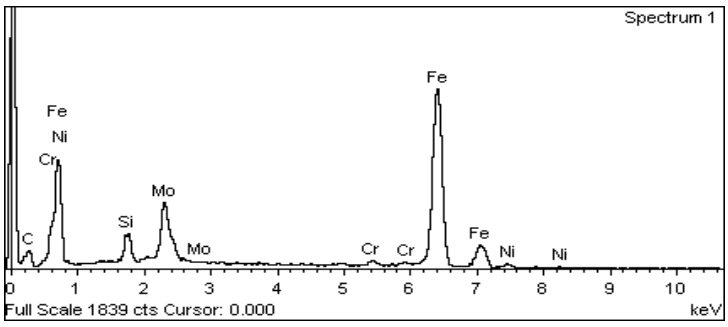

c)

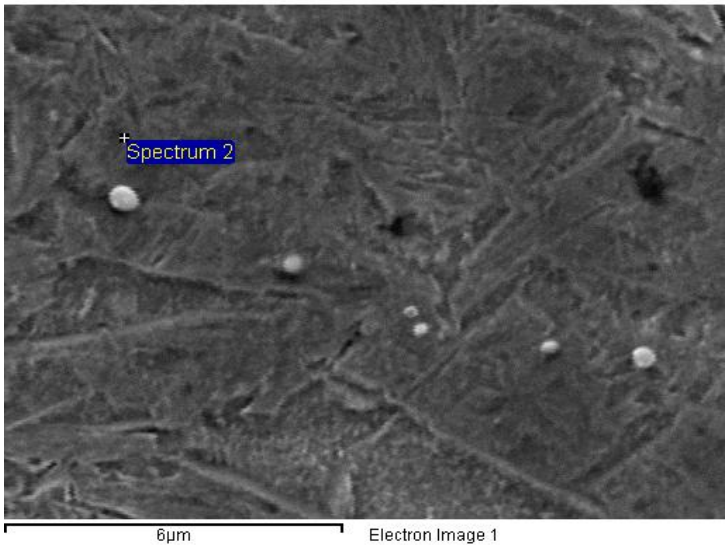

d)

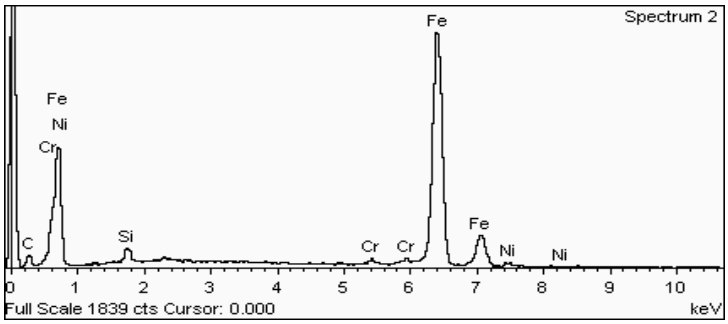

Figure 4.5 a) Mo-rich particle; b) EDS spectrum from Mo-rich particle; c) surrounding matrix for particle in a); and d) EDS spectrum from surrounding matrix for particle in a).

Table 4.2 Summary of number density (N_d) and volume fraction (V_f) of fine particles.

	Heat treatment	Number density, N_d per mm^2	Volume fraction, V_f
1.	925 ºC 1h AC	4939	0.000375
2.	925 ºC 1h WQ	2996	0.000167
3.	925 ºC 2h WQ	4858	0.000123
4.	925 ºC 4h WQ	2996	0.000172
5.	1025 ºC 2h WQ	2672	0.000108
6.	1025 ºC 2h AC	4777	0.000131
7.	870 ºC 1h OQ after 925 ºC 1h AC	5749	0.000417
8.	870 ºC 1h OQ after 1025 ºC 2h AC	6419	0.000110

Figure 4.6 shows the evolution of number density (N_d) and volume fraction (V_f) of Mo-rich particles with the heat treatment conditions. It can be seen that temperature and cooling rate have a significant effect on total particle volume fraction, $V_{f,}$ and number density, N_d. An increase in the austenitisation temperature from 925 ºC to 1025 ºC and increase in cooling rate for water and oil quenching as compared to air cooling resulted in lower overall volume fraction values, with 870 ºC 1h OQ after 1025 ºC 2h AC having one of the smallest volume fraction values but the largest overall number density.

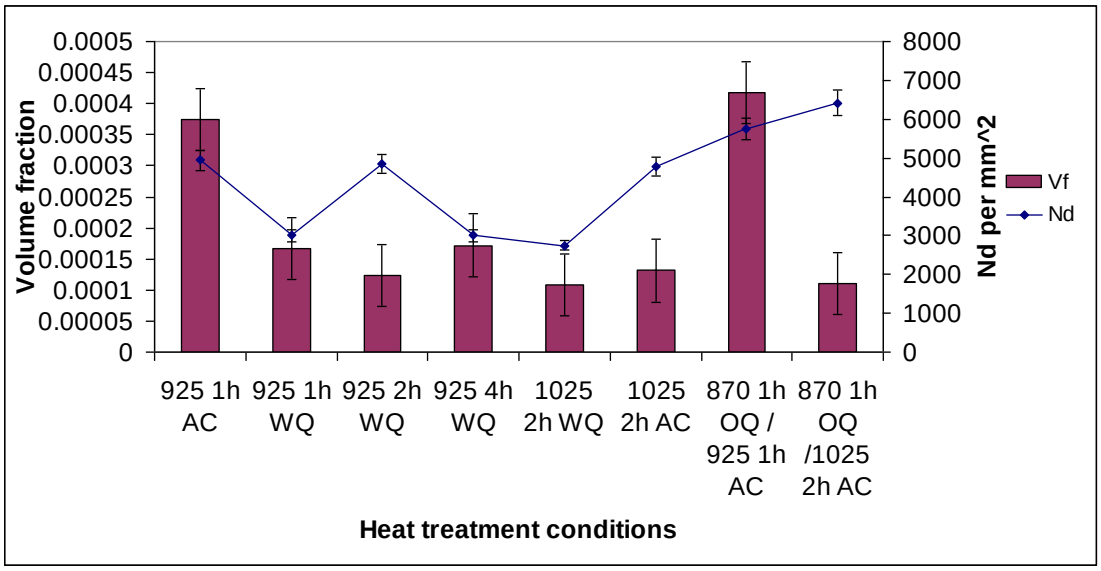

Figure 4.6 Variation of number density N_d and volume fraction V_f and with heat treatment.

4.2.1. Influence of 925 ºC temperature on fine Mo-rich particles

The effect of this austenitisation temperature on fine Mo-rich particles was studied by heating a sample to 925 ºC, holding for one hour and then water quenching. In comparison to 925 ºC 1h AC the total volume fraction decreased from 0.000375 to 0.000167 for 925 ºC 1h WQ, a reduction of approximately half, as a result of rapid cooling that reduced further precipitation during cooling, Table 4.2.

Figure 4.7 shows that the major contribution to the overall volume fraction for 925 ºC 1h WQ is given by particles in the 200-300 nm size range, whereas for 925 ºC 1 h AC it is the 400-500 nm size range that contributes the most to the total volume fraction.

The total number density value for 925 ºC 1h WQ decreased to 2996 mm^{-2} compared to 925 ºC 1 h AC condition of 4939 mm^{-2}, Table 4.2. It can be seen from Figure 4.7 that for 925 ºC 1 h WQ number density values show a decrease in all size ranges > 200 nm, with the major difference being in the > 300 nm particle size range.

Increasing holding times from 1 h to 4 h at 925 ºC has little effect on the total volume fraction, Figure 4.6, with particles in the 200-300 nm size range having the greatest contribution to the total volume fraction for the 1 h and 2 h holding times, and 500 - 600 nm size range for the 4 h holding time, Figure 4.7.

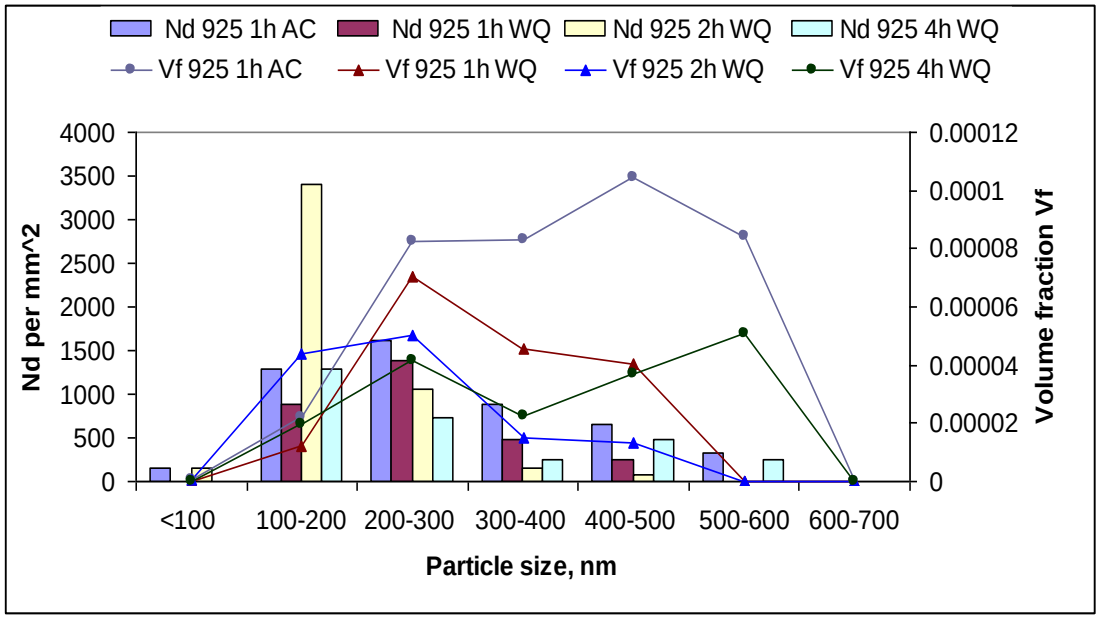

Figure 4.7 Number density and volume fraction as a function of particle size for heat treatments 1, 2, 3 and 4, Table 4.2.

4.2.2 Influence of 1025 ºC temperature on fine Mo-rich particles

An increase in the austenitisation temperature from 925 ºC to 1025 ºC resulted in increased dissolution of Mo-rich particles, increasing the amount of carbon and alloying elements in solution and increasing the hardenability of the steel, section 4.3.2.

The effect of 1025 ºC austenitisation temperature was analysed by heating the sample to 1025 ºC, holding for two hours and then water quenching.

The higher austenitisation temperature of 1025 ºC with 2h holding time resulted in a reduced total volume fraction value of 0.000108 compared with 0.000167 for 925 ºC 1h, Table 4.2, but with total number density values similar for both conditions.

As increased holding times from 1 to 4 h for 925 ºC austenitisation temperature had little effect on the total volume fraction, and considering the scatter in the measurements of volume fraction (volume fraction values for 925 ºC 2 h WQ and 1025 ºC 2h WQ are similar), Figure 4.6, it was the 1 h holding time for 925 ºC used

for comparison with 1025 ºC 2h. In addition, 1 h being the holding time for 925 ºC in the standard heat treatment SHT, Figure 4.2 (a).

Figure 4.8 shows the variation of volume fraction and number density values with particle size ranges on air cooling (AC) for 925 ºC 1h and 1025 ºC 2h heat treatments. It can be seen that for 1025 ºC 2h AC in the > 200 nm size range the N_d value showed a decrease, but they showed an increase for < 100 nm and 100-200 nm size ranges which would result from larger partially dissolved particles. The major contribution to the total number density value for 1025 ºC 2h AC is given by particles in the 100-200 nm size range whereas for 925 ºC 1h AC it is the 200-300 nm size range that gave the highest contribution to the total number density value, Figure 4.8. Although the total number density values for the two heat treatments (1) and (6) are similar, Table 4.2, the total volume fraction values show a major difference. For 1025 ºC 2h AC the total volume fraction decreased to 0.000131 from 0.000375 for 925 ºC 1h AC, 60% less, with particles in the finer size range, 200-300 nm, that contribute the most the total volume fraction value compared to 400-500 nm size range for 925 ºC 1h AC.

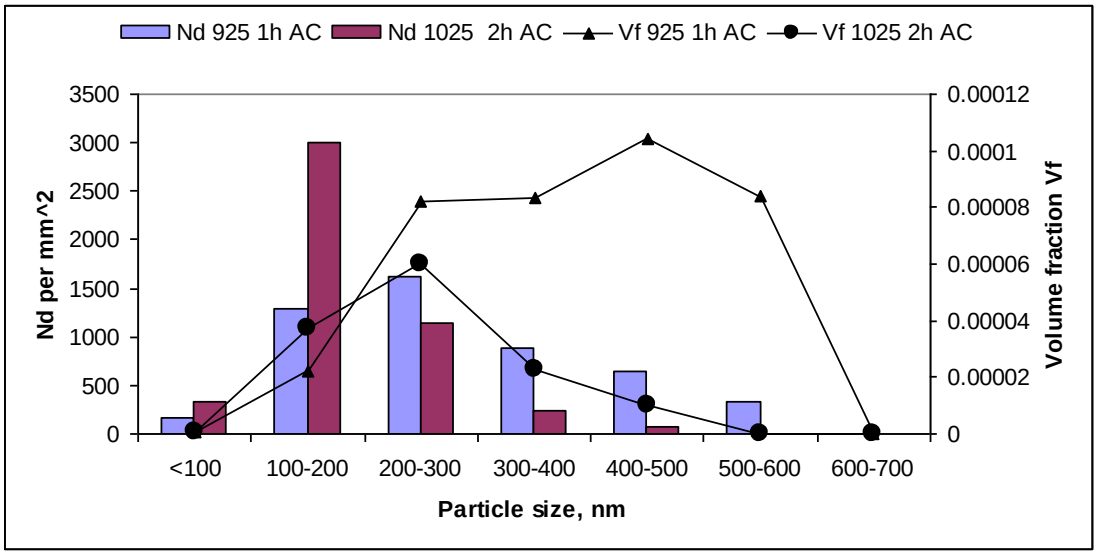

Figure 4.8 Number density and volume fraction as a function of particle size for heat treatments 1 and 6, Table 4.2.

4.2.3 Influence of 870 ºC temperature on fine Mo-rich particles

Austenitisation at 870 ºC for 1h followed by oil quenching after 925 ºC 1h AC and 1025 ºC 2h AC resulted in little change for the total volume fraction of Mo-rich particles, Table 4.2, 7 vs.1 and 8 vs. 6. In addition to that, at the end of 870 ºC stage the total N_d of Mo-rich particles for both conditions show a slight increase which is due to precipitation in the finer size ranges, Figure 4.9 and Figure 4.10, with particles in the 100-200 nm size ranges having the highest contribution to the total N_d for the two heat treatments, (7) and (8). The fine size of these precipitates contributes little to the total V_f and form due to the large undercooling, along with low diffusivity of Mo at 870 ºC for formation of Mo-rich particles.

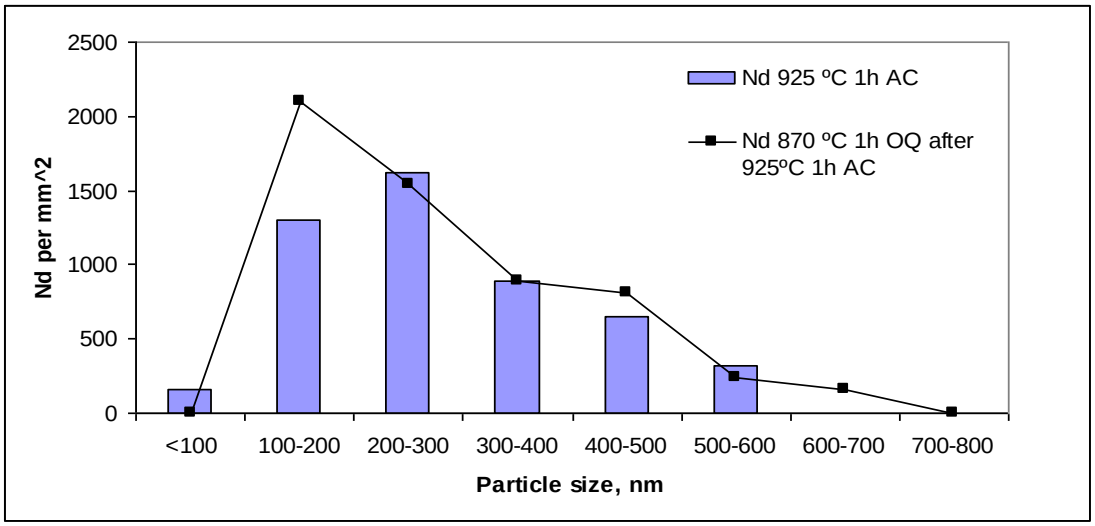

Figure 4.9 Number densities of fine particles as a function of size for heat treatments 1 and 7, Table 4.2.

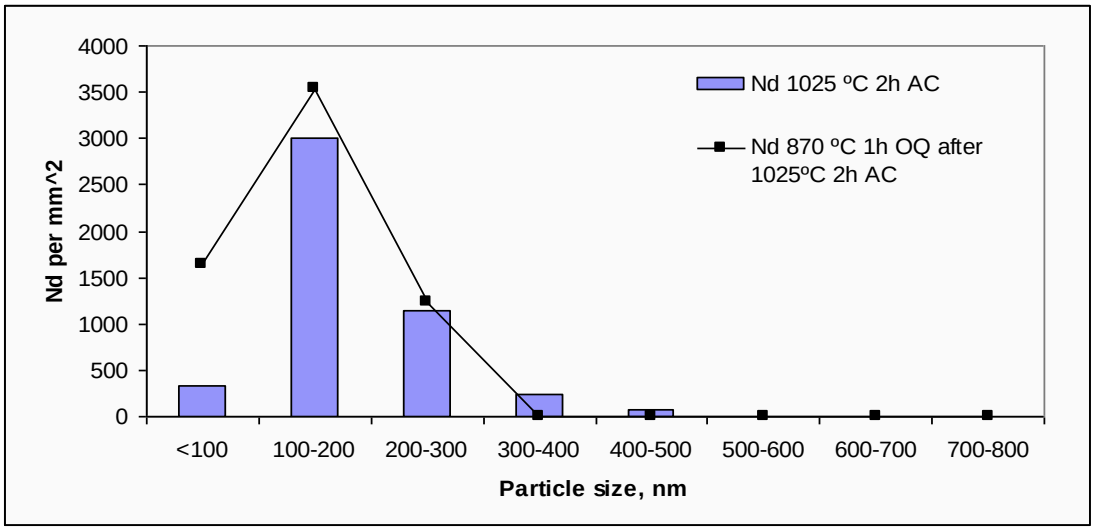

Figure 4.10 Number densities of fine particles as a function of size for heat treatments 6 and 8, Table 4.2.

It can be seen from Table 4.2 that 870 ºC 1h OQ after 1025 ºC 2h AC (8) in contrast to 870 ºC 1h OQ after 925 ºC 1h AC (7) resulted in changes in the total volume fraction, number density and size distribution, Figure 4.11, with heat treatment (8) having a total volume fraction reduced to 0.000110 from 0.000417 for heat treatment (7) as a result of the previous austenitisation at a higher temperature and a longer holding time. In addition to that, for heat treatment (8) particles in the finer size range, 200-300 nm, have the highest contribution to the total volume fraction, whereas for condition (7) it is the particles in the 400-500 nm size range that contribute most to the total volume fraction, Figure 4.11.

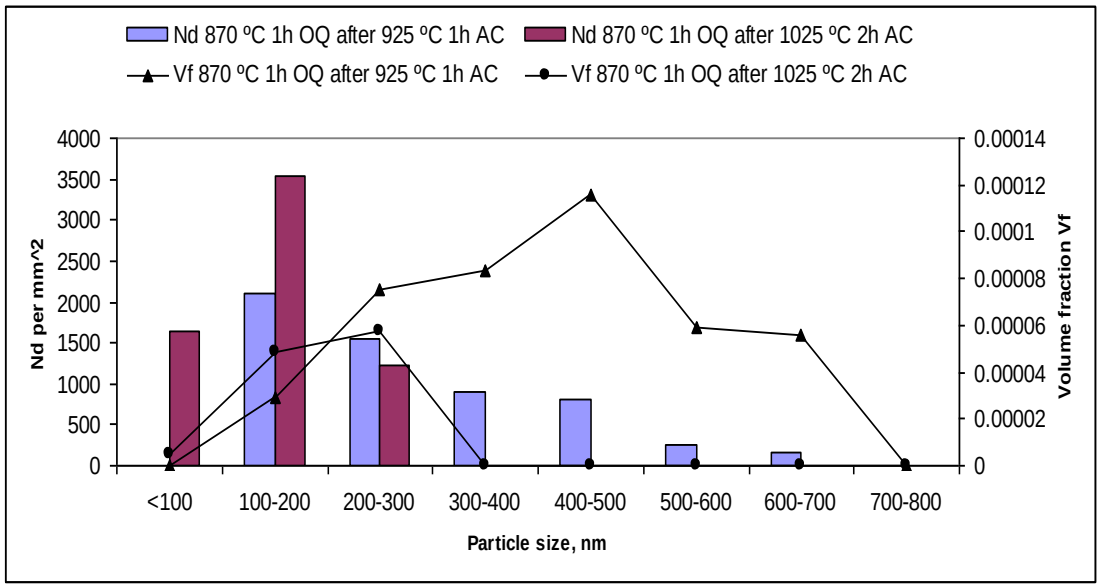

Figure 4.11 Number density and volume fraction as a function of particle size for heat treatments 7 and 8, Table 4.2.

Table 4.3 Measured and predicted volume fraction of Mo-rich particles.

Temperature	Measured V_f Mo-rich particles	Predicted V_f Mo-rich particles
925 ºC WQ	1.67×10^{-4}	7.7×10^{-5}
1025 ºC WQ	1.08×10^{-4}	4.5×10^{-5}

Table 4.3 compares the measured and predicted volume fraction values of Mo-rich particles at 925 ºC WQ and 1025 ºC WQ. The predicted volume fraction values of Mo-rich particles for both temperatures do not agree with the measured ones as the measured values exceed the predicted ones. The higher measured values may be associated with the scatter present in the measurement. Figure 4.4 (b), section 4.1, shows the elemental variation within the complex carbide with temperature.

4.3 Effect of heat treatment on hardness

The influence of various heat treatment conditions on steel microstructure (bainite fraction, particle distribution) and hardness was studied. Hardness dependence on particle distribution was not analysed due to particle size range being > 100nm, which are not likely to influence dislocation slip [Gladman, 1997]. Table 4.1 shows the evolution of macrohardness values and percentage of upper bainite in samples from steel D for the different heat treatments used in this study. Upper bainitic phases were more easily distinguished (as upper bainite is coarser than lower bainite) and separated from lower bainitic and martensitic phases. Upper bainite was quantified by measuring the area fraction, therefore, the percentage of upper bainite was used to analyse the effect of the heat treatment on matrix microstructure. The ranges of upper bainite produced by heat treatment are shown in Fig. 4.12; 25.65 % for heat treatment (6) and 11.18 % for heat treatment (7), (Table 4.4). Fig. 4.13 shows the variation of hardness with the heat treatments studied, the variation of upper bainite percentage with the heat treatment conditions is shown in Fig. 4.14 whereas the link between heat treatment conditions, percentage of upper bainite and macrohardness is shown in Fig.4.15.

Table 4.4 Values of hardness and upper bainite percentage of the different heat treatments studied for steel D, Figure 4.16.

	Heat treatment	Hardness HV_{10}	Percentage of upper bainite, %
1.	925 ºC 1h AC	638	17.60
2.	925 ºC 1h WQ	686	12.98
3.	925 ºC 2h WQ	684	15.25
4.	925 ºC 4h WQ	689	14.47
5.	1025 ºC 2h WQ	703	17.64
6.	1025 ºC 2h AC	669	25.65
7.	870 ºC 1h OQ after 925 ºC 1h AC	682	11.18
8.	870 ºC 1h OQ after 1025 ºC 2h AC	671	15.84
9.	300 ºC 2h AC *2	601	12.89

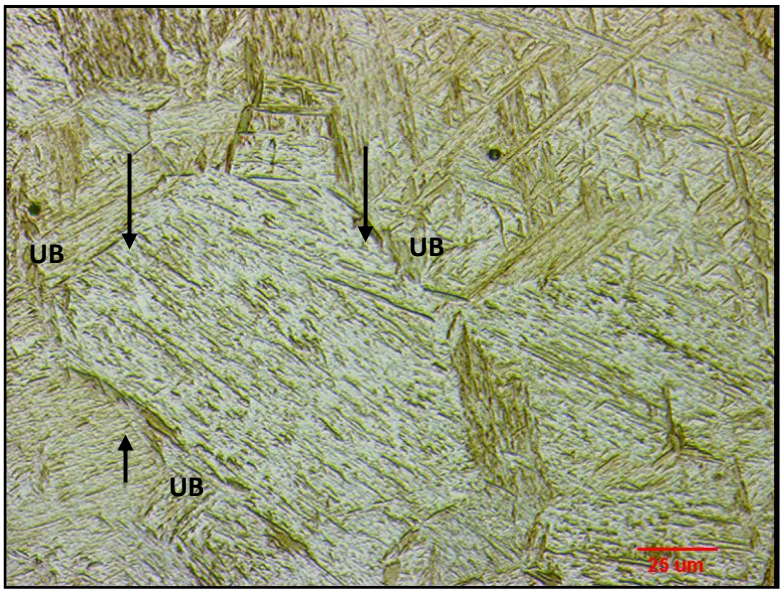

(a)

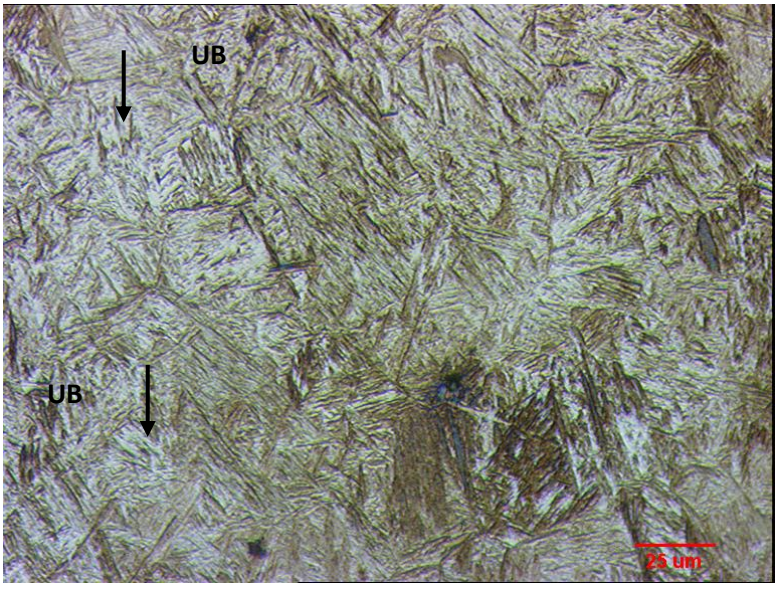

(b)

Figure 4.12 Optical micrographs of steel D showing the ranges of upper bainite (UB) produced by the heat treatments: (a) for 1025 ºC 2h AC (6) and (b) for 870 ºC 1h OQ after 925 ºC 1h AC (7), Table 4.2.

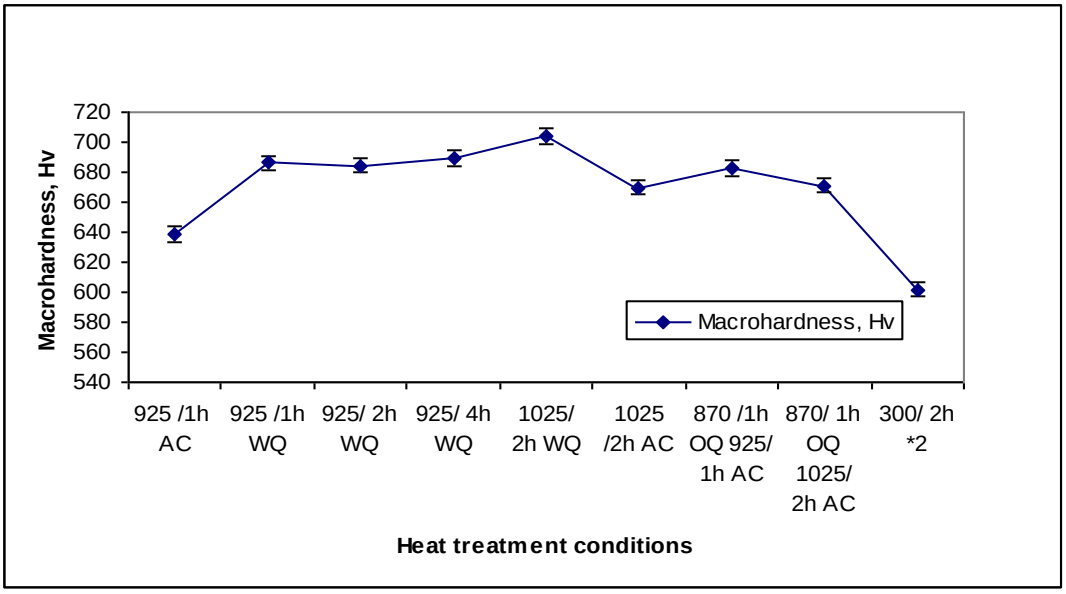

Figure 4.13 Variation of macrohardness with different heat treatment conditions.

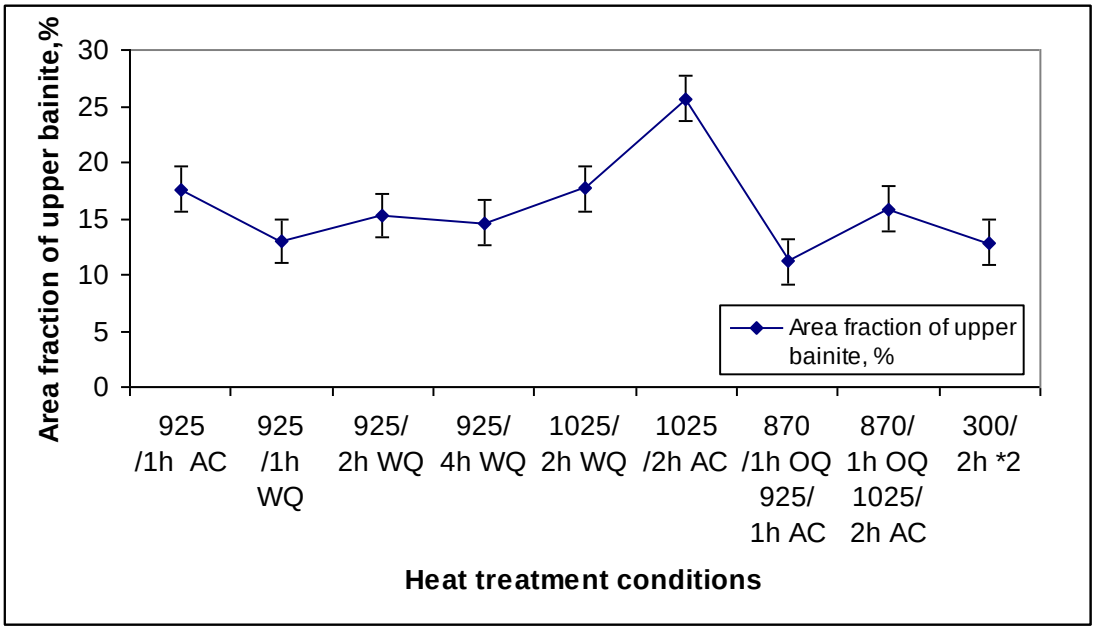

Figure 4.14 Variation of area fraction of upper bainite with different heat treatment conditions.

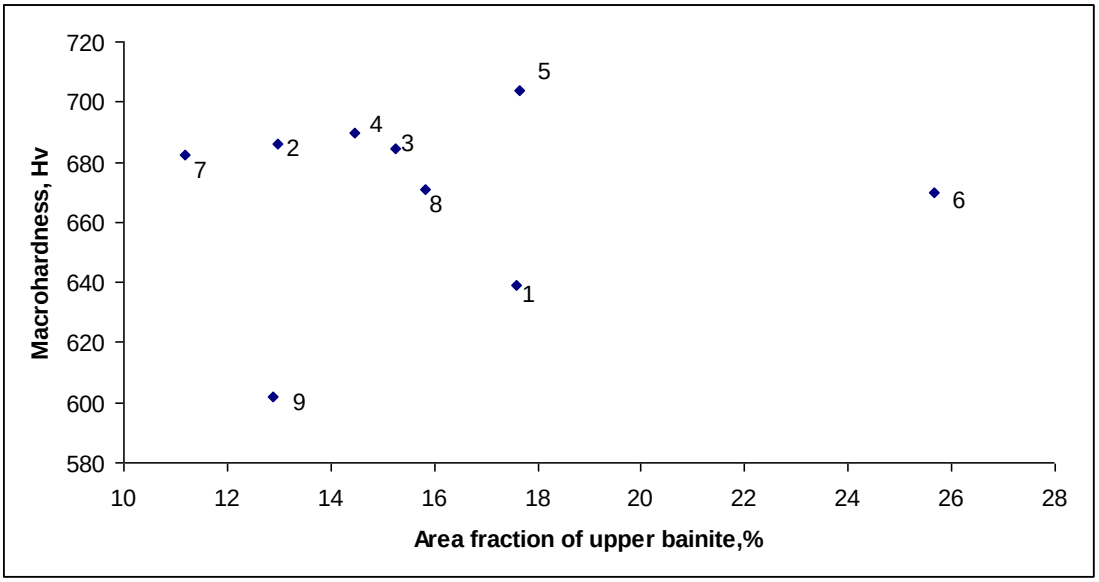

Figure 4.15 Variation of macrohardness and percentage of upper bainite with the heat treatments studied.

4.3.1 State of material at 925 ºC

The initial stage of the standard heat treatment, Fig. 4.16 (a), 1h austenitisation at 925 ºC, causes some of the pre-existing coarse Mo-rich particles to dissolve. In order to investigate the effects of 925 ºC 1h austenitisation, the sample was water quenched. For 925 ºC 1h WQ the hardness increased to 686 Hv from 636 Hv for the 925 ºC 1h AC, this is due to rapid cooling that minimised the extent of carbo-nitride precipitation.

Table 4.5 shows that the total N_d of particles for 925 ºC 1h WQ is low (2996) compared to 925 ºC 1h AC (4939). The major difference is given by the larger particle size range: 300-400 nm with a N_d of 408 compared to 890, 400-500 nm with a N_d of 242 compared to 647, Fig. 4.17. No particles of the size range 500-600 nm were observed for the water quenched sample. In addition, the total volume fraction of Mo-rich particles was reduced for the 925 ºC 1h WQ sample to 0.00016 from 0.00037 for the 925 ºC 1h AC, Fig. 4.18.

As a result of water quenching more carbon is retained in solution, so that more lower bainite and martensite form, which have a higher carbon content leading to the

increase in hardness, Fig.4.13. The formation of more lower bainite explains the decrease in the percentage of upper bainite to 12.98 % for the water quenched sample compared to 17.60 % for the air cooled one, Fig. 4.14. Water quenching produced a bainitic/martensitc microstructure, Fig. 4.19 (a), whereas air cooling produced a more upper bainitic microstructure, Fig. 4.19 (b).

Increasing holding times from 1h to 4h at 925 ºC followed by water quenching has no significant effect on particles, Fig. 4.18, percentage of upper bainite, Fig. 4.14, or hardness, Fig. 4.13.

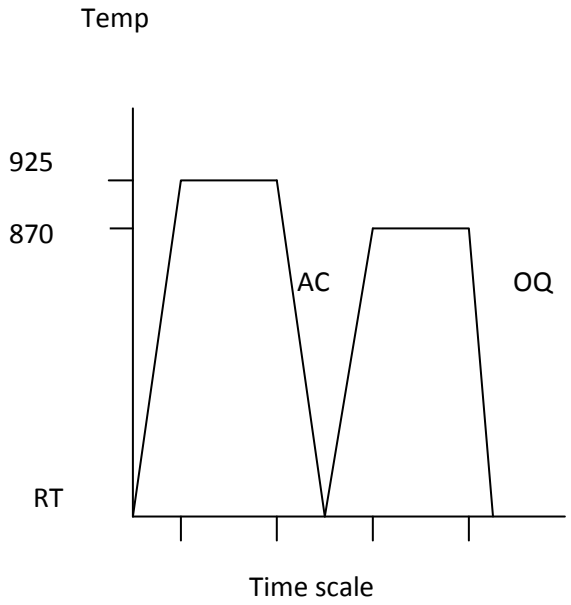

a)

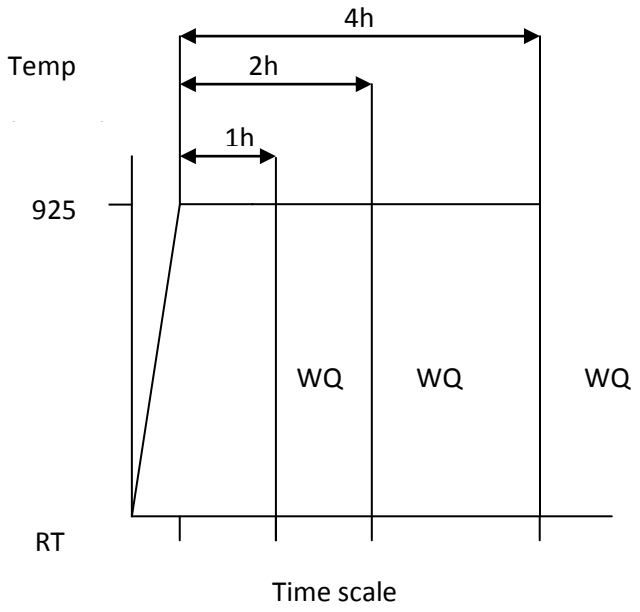

b)

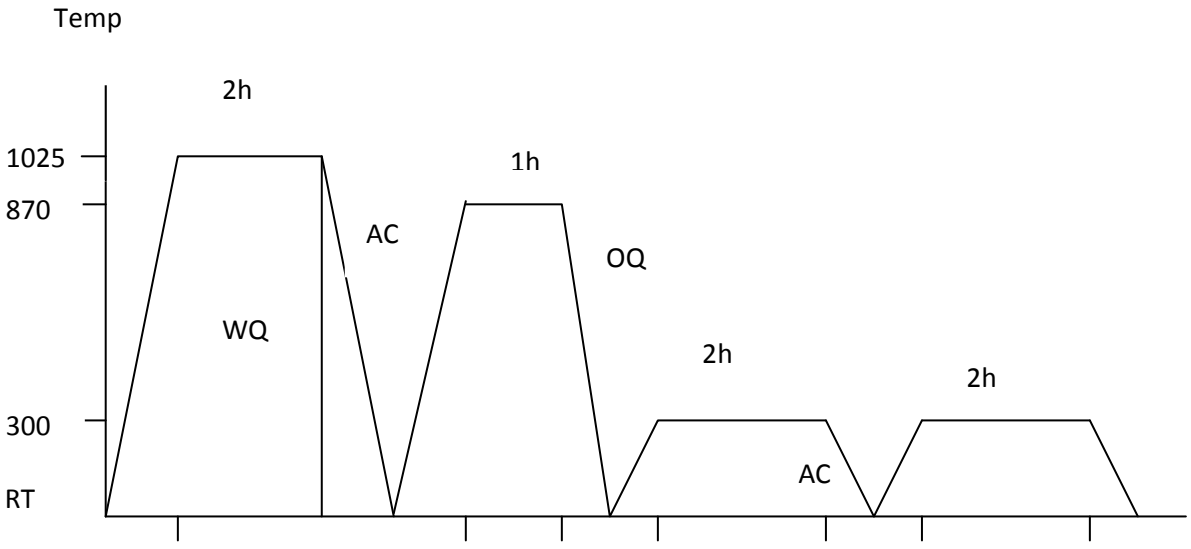

c)

Figure 4.16 Schematic diagram of heat treatments: (a) standard heat treatment (SHT); (b) trial heat treatment 1; and (c) trial heat treatments 2, 3 and 4 (Table3.2).

Table 4.5 Number densities of Mo-rich particles, N_d, (mm^{-2}) for 925 °C heat treatment conditions

Size	**N_d, 925 1h AC**	**N_d, 925 1h WQ**	**N_d , 925 2h WQ**	**N_d, 925 4h WQ**
	Total N_d=4939	Total N_d=2996	Total N_d=4858	Total N_d=2996
<100 nm	161	0	161	0
100-200 nm	1295	890	3401	1295
200-300 nm	1619	1376	1052	728
300-400 nm	890	485	161	242
400-500 nm	647	242	80	485
500-600 nm	32	0	0	242
600-700 nm	0	0	0	0

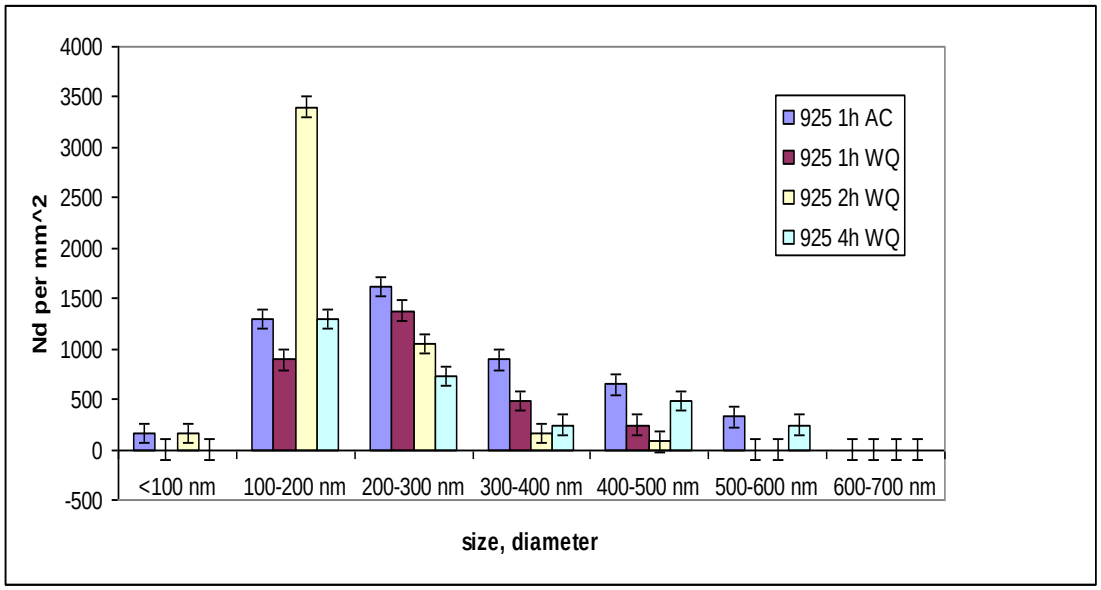

Figure 4.17 Number densities of Mo-rich particles as a function of size and heat treatment conditions: 1, 2, 3 and 4, Table 4.5.

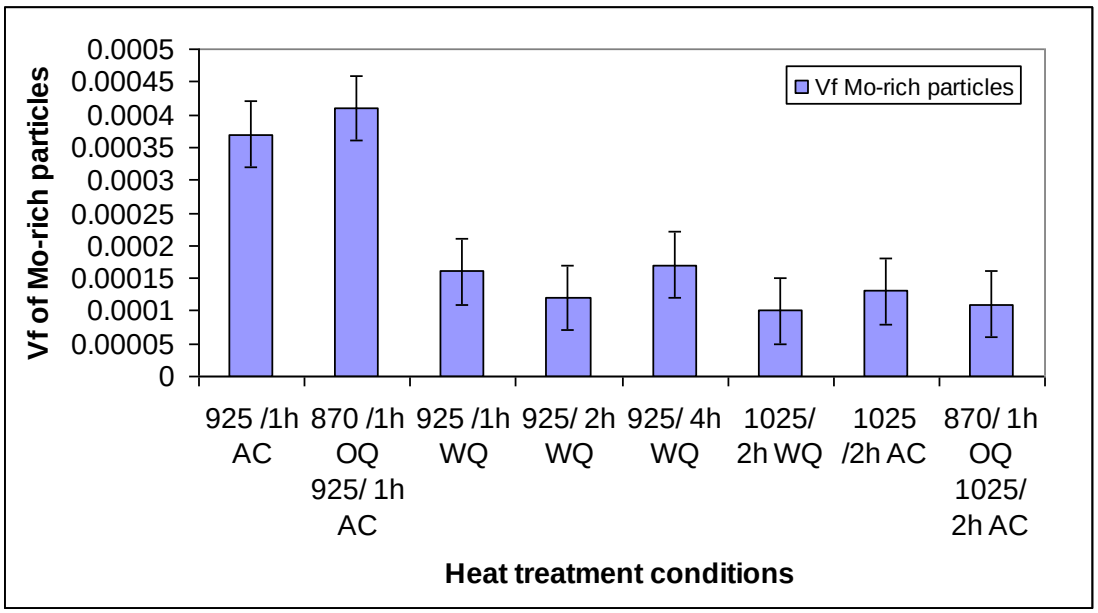

Figure 4.18 Volume fraction of Mo-rich particles for the heat treatments studied.

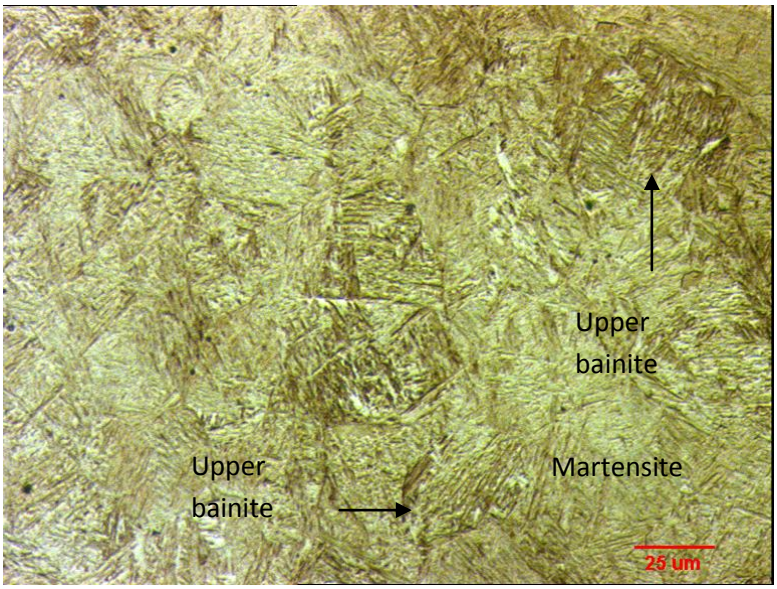

a)

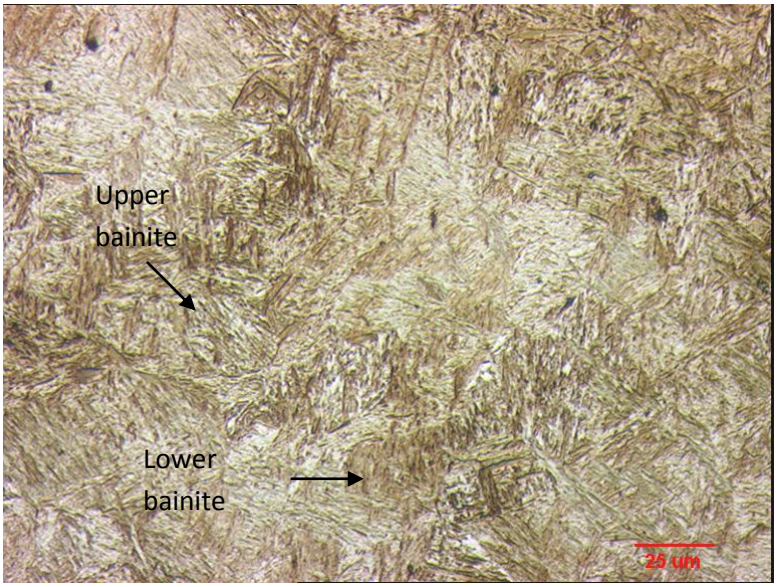

b)

Figure 4.19 Optical micrographs showing: (a) bainitic/martensitic microstructure for 925 °C 1h WQ and (b) bainitic microstructure for 925 °C 1h AC.

4.3.2 State of material at 1025 ºC

By increasing the austenitising temperature from 925 ºC to 1025 ºC with a holding time of 2 h more Mo-rich particles were dissolved, Fig. 4.18, changing the amount of carbon and alloying elements in solution and increasing the hardenability of the steel, therefore, the nose of the "C"-curve on the TTT diagram will be displaced to the right and the Ms temperature will be lowered, Fig. 4.20 (b). This should give a decrease in the percentage of upper bainite (not seen) and increase in hardness (seen) (Table 4.4).
In order to analyse the effect of the austenitisation temperature, 1025 ºC for a 2 h holding time, the sample was water quenched. It can be seen from Fig. 4.18 that the volume fraction of the Mo-rich particles decreased in comparison with 925 ºC WQ, and the macrohardness value was the highest recorded at 703 Hv, Table 4.4. The hardness dropped to 669 Hv when the sample was air cooled (6) as a result of the precipitation that occurred during cooling, thus the volume fraction of the Mo-rich

particles increased in comparison with 1025 ºC 2h WQ (5), Fig. 4.18. Water quenching resulted in a lower percentage of upper bainite than air cooling, as water quenching retains more carbon in solution, so that more lower bainite and martensite forms and less upper bainite.

4.3.3 Comparison between 925 ºC and 1025 ºC

Austenitisation at 925 ºC 1h followed by air cooling resulted in a lower hardness, as shown in Table 4.4, than 1025 ºC 2h AC. The 925 ºC austenitisation temperature has the disadvantage of a higher volume fraction of undissolved Mo-rich particles compared to 1025 ºC temperature. In addition to that, further precipitation during the air cooling takes more carbon out of the solution, explaining why the hardness of the resulting microstructure was lower than 1025 ºC 2h AC. The higher austenitisation temperature offers the possibility of dissolving a higher volume fraction of Mo-rich particles, so that the resulting volume fraction of the precipitates after air cooling is lower than 925 ºC. Figure 4.18. For 1025 ºC austenitisation temperature the increased level of C in solution shifted the "C"-curve to the right and Ms temperature was reduced. In contrast to 925 ºC 1h AC, 1025 ºC 2h AC produced a higher percentage of upper bainite as a consequence of its effect on the hardenability of the steel, Table 4.4. Superimposing cooling curves on the TTT diagrams, Fig. 4.20 (a) and (b) explains the steel responses to 925 ºC 1h AC and 1025 ºC 2h AC regarding the increased percentage of upper bainite for the latter temperature. Comparison of the Fig. 4.20 (a) and (b) shows that the cooling curve 1_b crosses the beginning of the transformation at point $x1_{b,}$ with the formation of upper bainite, at a longer time then cooling curve 1_a, slowing down the kinetics and as a result there is more time for the formation of upper bainite for 1025 ºC 2h AC. Transformation will continue until point $x'1_b$ when it finishes with the formation of lower bainite.

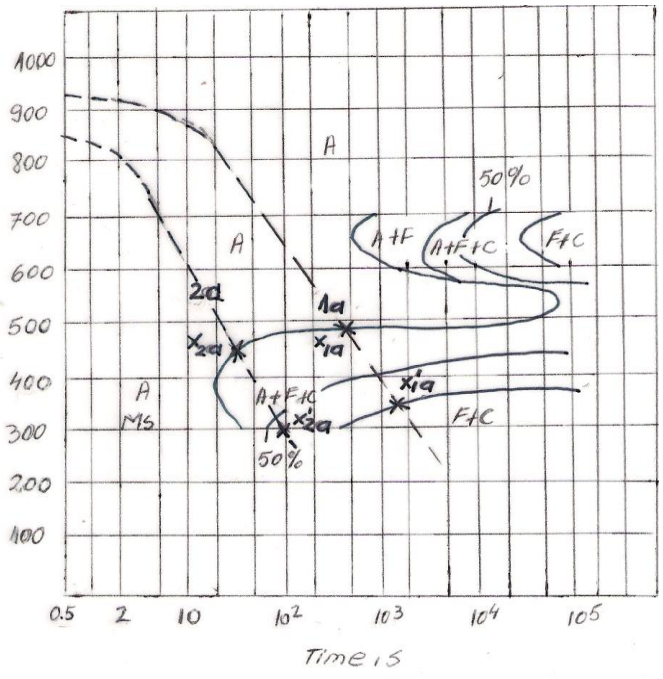

a)

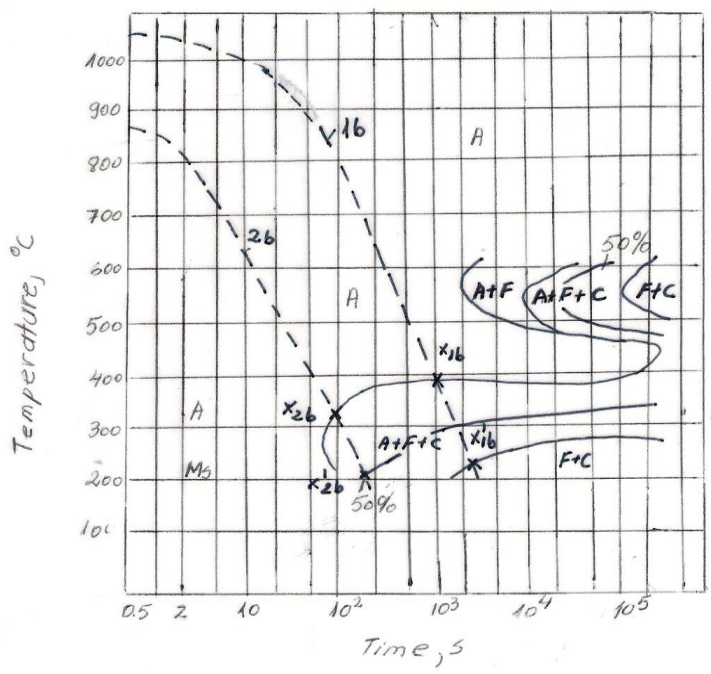

b)

Figure 4.20 Schematic TTT curve for 300M specification [Felice & Pritchard, 1998]: (a) 925 ºC austenitisation temperature; (b) 1025 ºC austenitisation temperature. Cooling curves 1_a and 1_b represent air cooling; cooling curves 2_a and 2_b represent oil quenching.

4.3.4 Variations at 870 ºC 1h OQ

A comparison of the results obtained in quenching the specimens after 925 ºC 1h AC, (7), and 1025 ºC 2h AC,(8), shows a decrease in macrohardness from 682 Hv to 671 Hv, Fig. 4.13, furthermore, the percentage of upper bainite increased slightly from 11.18 to 15.84 %, Fig. 4.14. The drop in macrohardness for 870 ºC 1h OQ after 1025 ºC 2h AC, (8), compared to 870 ºC 1h OQ after 925 ºC 2h AC, (7), resulted from an increased percentage of upper bainite. What is more, the volume fraction of precipitates also accounts for this, the first oil quenching (7), resulted in a higher volume fraction of undissolved Mo-rich particles inherited from 925 ºC 1h austenitisation followed by air cooling, reaustenisation at 870 ºC for 1h leaving more undissolved particles prior to oil quenching compared to second oil quenching (8). At 1025 ºC austenitisation temperature with 2 h holding time more carbon and alloying elements are released into solution, due to greater dissolution of precipitates, changing the hardenability that would result in modifications in the matrix microstructure. Cooling curve 2_a crosses the beginning of the transformation at a shorter time than $2_{b,}$ Figure 4.20 (a) and (b), less time being allowed for the transformation, which explains the decrease in the percentage of upper bainite for the first quenching after 925 ºC 1h AC. The second quenching, 870 ºC 1h OQ after 1025 ºC 2h AC, resulted in a significantly lower volume fraction of undissolved particles due to the higher austenitisation temperature and longer holding time, macrohardness value for the latter being the result of more carbon in solution rather than precipitates.

4.3.5 Tempering

On double tempering at 300 ºC for 2h after 870 ºC 1h OQ for 1025 ºC 2h AC (Figure 4.16) the hardness drops to 601 Hv from 671 Hv for the as-quenched specimen, Table 4.4. The decrease in hardness is due to the response of martensite to tempering, as the trapped carbon in the supersaturated solution would precipitate, whereas the tempering of bainite is not expected to influence it [Bhadeshia, 2001], in addition, the percentage of upper bainite is similar to the as-quenched condition.

In comparison with behaviour at 925 ºC 1h/ AC/870 ºC 1h/OQ when the hardness decreases to 603 Hv (Berry, 2001) from 682 Hv (Table 4.1), the drop in hardness is lower for 1025 ºC 2h AC/870 ºC 1h/ OQ after double tempering.

The response to tempering is explained by the fact that the percentage of upper bainite for the as-quenched specimens is different: 15.84 % for the 1025 ºC austenitised sample and 11.18 % for the 925 ºC austenitised one. As a result the 925 ºC austenitised sample has more lower bainite and martensite and therefore a greater tempering response than the 1025 ºC austenitised specimen.

4.4 Effect of austenitisation temperature on toughness

Fracture toughness results (K_Q values) obtained from CT specimens for the two heat treatments are shown in Table 4.6, with higher austenitisation treatment, heat treatment 2, resulting in a higher fracture toughness value. Heat treatment schedules for fracture toughness testing are shown in Table 3.3, section 3.

Table 4.6 K_Q values of the two heat treatments.

	Heat treatment	K_Q MPa$\sqrt{m}$
1.	925 ºC	63.90
2.	1025 ºC	65.97

Fractographic examination from fractured CT specimens for the two heat treatments was carried out using SEM. Examples of the fracture sequence for the two conditions are shown in Fig. 4.21(a) and (b).

It can be seen that the fracture surfaces consisted predominantly of a fine dimple fracture with local cleavage facets for the zone ahead of the fatigue precrack, for both conditions, failure occurring by ductile (microvoid coalescence) mechanism.

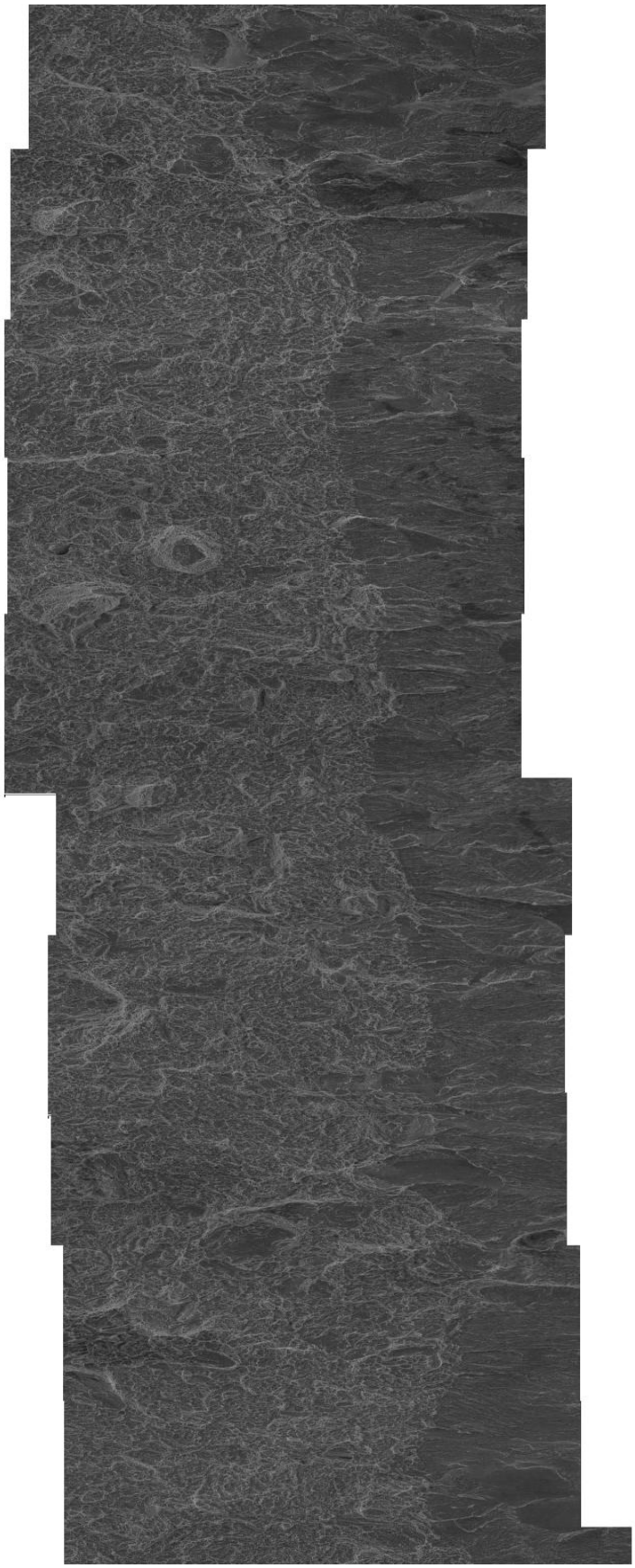

a)

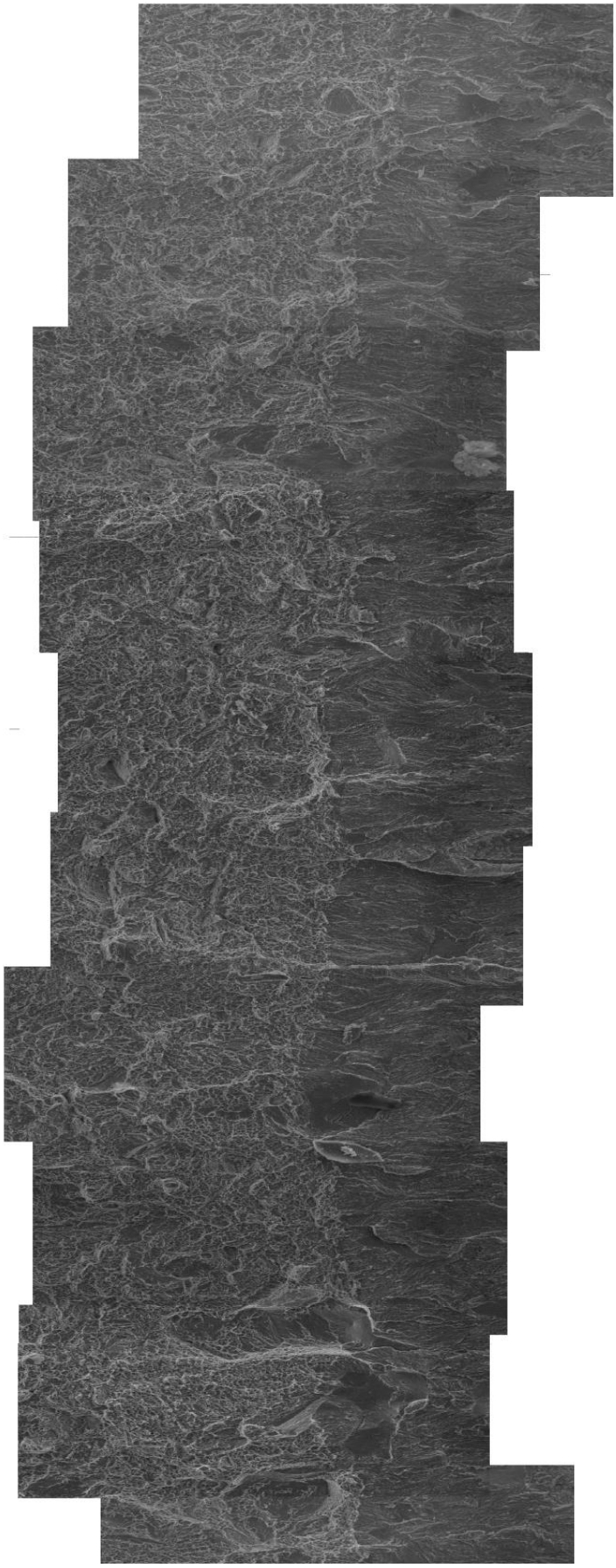

b)

Figure 4.21 Fracture sequence of the initiation zone for the two conditions including the prefatigue front on the right hand side: a) heat treatment 1 and b) heat treatment 2, Table 4.6.

Qualitatively Fig. 4.21 (a) seems flatter with a higher proportion of facets than Fig. 4.21 (b), consistent with K_Q values.

In the fracture surfaces examined, coarse particles, TiN and MnS, appeared not to have an effect on the initiation of failure, being associated with large isolated voids, Fig. 4.22. Coarse particles, have a higher probability of containing a larger internal defect, will initiate void by cracking and / or decohering. The formation of voids around cracked and decohered particles blunts microcracks and cleavage initiation does not occur.

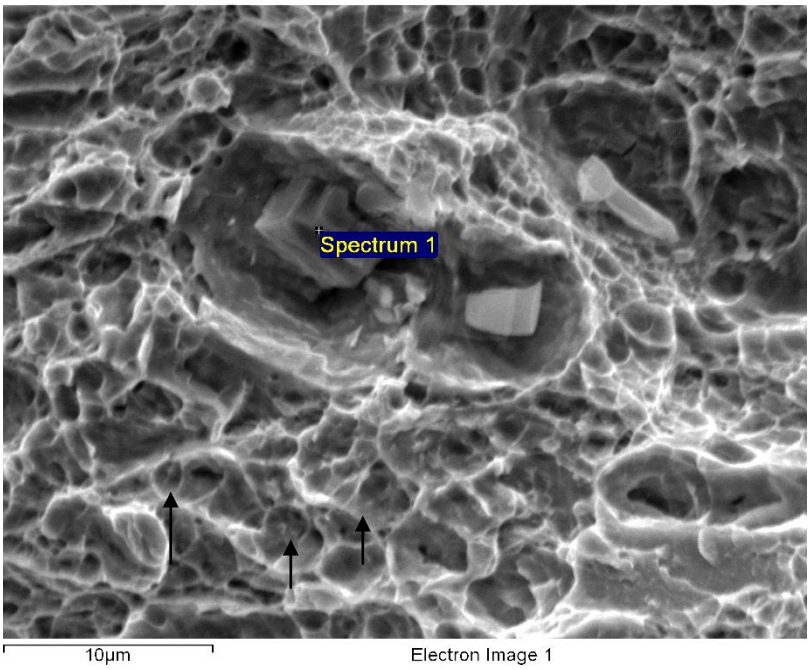

Figure 4.22 Ductile failure in the fracture surface for heat treatment 1 showing large voiding around a MnS particle (~ 4 µm) and a broken TiN particle (6 µm) with secondary voiding around fine particles, arrowed.

The higher austenitisation temperature of 1025 °C with 2h holding time resulted in a reduced volume fraction of fine particles compared with 925 °C, but increased number density value, Table 4.2, heat treatments 7 and 8, section 4.3. Also, the

volume fraction of fine particles for 1025 °C was dominated by particles in the smaller size range (200 - 300 nm) and complete dissolution of particles > 300 nm compared with 925 °C, which was dominated by particles in the larger size range (400 - 500 nm).

Examples of dimple size distributions for heat treatment 1 and heat treatment 2 are shown in Figure 4.23 (a) and (b).

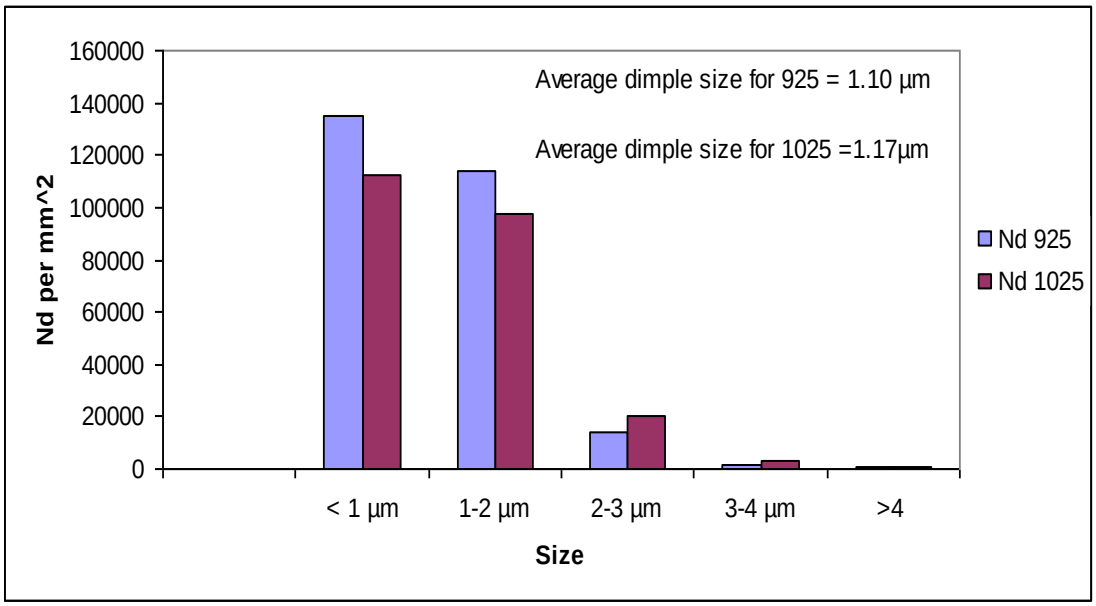

a)

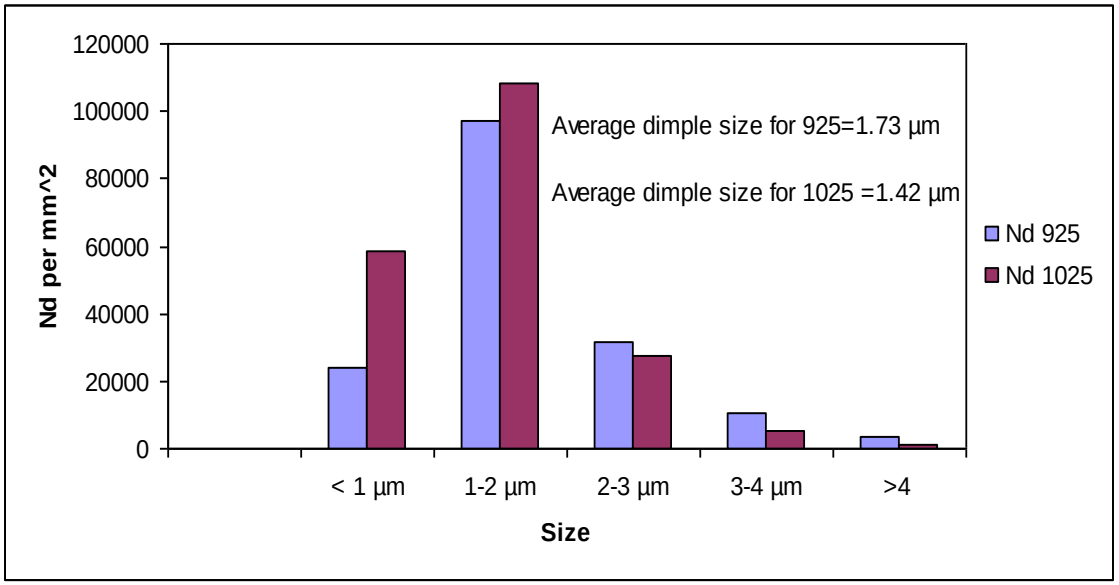

b)

Figure 4.23 Number densities as a function of dimple size for heat treatment 1 and heat treatment 2: a) initiation zone and b) beyond the initiation zone, in the first half of the fracture zone.

In the initiation zone, the average dimple size was 1.10 μm for 925 ºC heat treatment and 1.17 μm for 1025 ºC heat treatment. The effect of higher austenitisation temperature can be better noticed for the second dimples, beyond the initiation zone in the first half of the fracture zone, where the average dimple size has reduced from 1.73 μm for heat treatment 1 to 1.42 μm for heat treatment 2 due to higher number density and reduced volume fraction of particles.

Small particles initiate voids at very high strains and the strain required for void initiation increases with particle size decreasing.

By minimising the volume fraction and increasing the number density the structure is dominated by a greater number of fine particles, the plastic energy is dissipated in many small microvoids so that large voids are not favoured, and fracture toughness is improved.

The improved fracture toughness resulted from modified size distribution of fine particles and changed microstructure with higher austenitisation temperature, as 1025 ºC heat treatment resulted in an increased percentage of upper bainite, 15 % , in comparison to 11 % for 925 ºC heat treatment, so less martensite, leading to increased plasticity and explaining the improved fracture toughness.

CHAPTER 5
Conclusions and Further work

5.1 Conclusions

The effect of different austenitisation temperatures with different holding times on the particle distributions and matrix microstructure in one cast of 300M steel have been studied.

The major findings are as follows:

- Coarse TiN particles, which were identified and quantified by image analysis, formed during liquid phase processing of the steel were not affected by subsequent heat treatments with the V_f and N_d values not being noticeably different.
- 925 °C austenitisation temperature for increasing holding time from 1h to 4h has no significant effect on fine particles (<600 nm), percentage of upper bainite and hardness.
- 1025 °C austenitisation temperature with a holding time of 2h resulted in a decreased volume fraction of fine particles, 60 % less than 925 °C SHT austenitisation temperature, also changing the size distribution, with particles in the finer size range, 200-300 nm, dominating the volume fraction compared to 400-500 nm size range for 925 °C austenitisation temperature.
- The higher austenitisation temperature was effective in improving the fracture toughness value by 2 MPa $m^{1/2}$ compared to SHT austenitisation temperature, and it is attributed to increased dissolution of fine particles.

5.2 Further work

As the austenitisation temperature is not the only factor controlling the fracture toughness, in order to improve fracture toughness keeping the same strength the influences of matrix microstructure such as: retained austenite, the shape and size of lower bainite and martensite needs to be considered.

REFRENCES

1. Tomita Y. Materials Science and Technology, 1995, Vol. 11, pp. 508 - 513.

2. Gladman T., The physical Metallurgy of Microalloyed Steels, The Institute of Materials, London, 1997.

3. Honeycombe R.W.K. and Bhadeshia H.K.D.H., 2end edition, Edward Arnold, 1995.

4. Cacknell A. and Petch N.J, Frictional forces on dislocation arrays at the lower yield point in iron, Acta Metallutgica, Vol. 3, March 1955, p. 186 – 189.

5. Orowan E., Internal Stress in metal and alloys, The Institute of Metals, London, 1948, No. 451.

6. Nicholson R.B., Strengthening Methods in Crystals, Ed. A. Kelly & R.B. Nicholson, Elsevier, Amsterdam, 1971, p. 535.

7. Tomita Y. and Okabayashi K., Metall. Trans. A., 1984, Vol.15A, pp. 2247 - 2249.

8. Porter D. A. and Easterling K.E., Phase Transformation in Metals and Alloys 2end edition, 1992.

9. Stevens W. and Haynes A.J. Iron Steel Inst., 1956, Vol.183, pp. 349 - 359.

10. Radcliffe S.V., Schatz M. and Kulin S.A., J. Iron Steel Inst., 1963, Vol. 201, pp. 143 - 153.

11. Horn R.M. and Ritchie R.O., Metall. Trans. 9A., 1978, pp.1039 – 1053.

12. Bhadeshia H.K.D.H. and Edmonds D.V., Met. Sci., September 1983, Vol. 17, pp. 411 - 419.

13. Oka M. and Okamoto H., Proc. Int. Conf. On Martensitic Transformations, ICOMAT., 1986, Japan Inst. Of Met. ,pp 271 – 275.

14. Sandvik B.P.J. and Nevalainen H.P., Met. Tech., 1981, Vol. 15, pp. 213 - 220.

15. Tomita Y., Materials Science and Technology, 1991, Vol. 7, pp 229 - 306.

16. Tomita Y. and Okawa T., Materials Science and Engineering A., 1993, Vol. 172, pp. 145 – 151.

17. Garrison W. M. and Wojcieszynski A. L., Mat. Sci. and Eng., 2007, Vol.464, 321 – 329.

18. Leslie W. C., ISS. Trans., 1983, Vol 2, pp. 1 - 24.

19. Tomita Y., Metall. Trans. A, 1990, Vol. 21A, pp. 2739 – 2746.

20. Tomita Y., Metall. Trans. A, 1988, Vol 19A, pp. 1555 – 1561.

21. Linaza M.A., Romero J.L., Rodriguez-Ibabe J. M. and Urcola J.J., Scripta Metall. et. Materialia, 1995, Vol. 32, No 3, pp.395 – 400.

22. Zhang L.P., Davis C.L. and Strangwood M., Metall. and Mater. Trans. A, 1999, Vol. 30A, pp. 2089 - 2096.

23. Balart M.J., Davis C.L. and Strangwood M., Mat. Sci. and Eng. A, 2000, Vol. 284, pp. 1 - 13.

24. Li J.Y. and Zhang W.Y., Journal of Iron and Steel Inst., 1989, Vol. 29, No. 2, pp. 158 - 164.

25. Leap M.J. and Wingert J.C., Metall. and Mater. Transactions. A, 1999, Vol. 30A, pp. 93 - 113.

26. Zhang L.P., Davis C.L., and Strangwood M., Metall. and Mater. Trans. A, 2001, Vol. 32A, pp. 1147 – 1155.

27. Gore M.J., Olson G.B. and Cohen M., Innovations in Ultrahigh – Strength Steel Technology, (Eds. Olson G. B., Azrin M. and Wright E. S.) Sagamore Army Materials research Conference proceedings, Watertown, 1987, pp. 425 – 441.

28. Tomita Y. and Okabayashi K., Metall. Trans. A., 1983, Vol. 14A, pp. 485 - 492.

29. Tomita Y. and Okabayashi K., Metall. Trans. A., 1985, Vol. 16A, pp. 73 – 82.

30. Youngblood J.L. and Raghavan M., Metall. Trans. A, September 1977, Vol. 8A, pp. 1439 – 1448.

31. Ritchie R.O., and Horn R.M., Metall. Trans. A., 1978, Vol. 9A, pp. 331 – 341.

32. Knott J. and Withey P., Fracture Mechanics Worked Examples, The Institute of Materials, London, 1998.

33. Berry J.E., PhD, University of Birmingham, 2001.

34. Chen B.F., Pan W.L., Yu G.P., Hwang J. and Huang H.J, Surface and Coatings Technology, Vol. 111, 1999, pp. 16 – 21.

35. Felice C. and Pritchard J.E., Adv. Mat. And Processes, 1998, Vol. 154, No. 4, pp. 191 - 196.

36. Pickering F.B. and Gladman T., Metallurgical Developments in Carbon Steels Iron and Steel Institute, Special Report No. 81, 1963, p.10.

37. Heslop J. and Petch N.J., Phil. Mag., 1957, 2, p.649.

38. Bhadeshia H. K. D. H., Bainite in Steels, 2end edition, The Institute of Materials, Minerals and Mining, 2001.